

Dynamical Cluster Assembly Framework (D-CAF): The Link Between Star Cluster Formation and Expansion Rates

JUAN P. FARIAS¹ AND ALISON SILLS¹

¹*Department of Physics and Astronomy, McMaster University, 1280 Main Street W, Hamilton, ON L8S 4L8, Canada*

ABSTRACT

We introduce the Dynamical Cluster Assembly Framework (D-CAF), an AMUSE-based framework designed to connect embedded star formation histories to the dynamical evolution of young stellar systems. We model star formation through the gradual formation of stars inside an evolving background potential, where the global gas evolution is extracted from realistic magneto-hydrodynamical (MHD) simulations. In this first work, we focus on the global evolution of the natal gas and its dynamical imprint on the stellar population. Across all explored MHD setups, we find that the gas continues to collapse while stars are forming, increasing both the central concentration and velocity scale of the embedded stellar population before gas expulsion. Using a controlled grid of direct N -body simulations, we show that this embedded evolution strongly regulates both the survival and later expansion of young stellar systems. In particular, gas contraction shortens the stellar crossing time prior to gas expulsion, making the same gas-removal timescale effectively more adiabatic for the stars. We find that the present-day expansion of stellar associations still preserves information about the embedded dynamical state reached during formation. The expansion rate is limited by the velocity scale reached before gas expulsion, while the efficiency with which this velocity field is transformed into expansion depends on the gas-expulsion timescale. Finally, we show that some commonly used expansion diagnostics can directly trace the physical expansion rate of young stellar systems when full kinematic information is available, opening the possibility of using stellar kinematics to constrain the dynamical conditions of embedded star formation.

1. INTRODUCTION

Most stars form in clustered environments, at densities far above the field, yet a large fraction of young stars are dispersed within only a few Myr (C. J. Lada & E. A. Lada 2003; E. Bressert et al. 2010; R. Pokhrel et al. 2020). Star formation takes place inside molecular clouds with intrinsically complex dynamics. The gas is turbulent and magnetised, strongly structured over a wide range of scales, and rapidly evolving under its own gravity and stellar feedback (M.-M. MacLow 2004; B. G. Elmegreen 2007). The interplay between these processes, and their relative importance across different environments, is therefore expected to play a crucial role in setting the early survival rate and kinematic properties of star clusters.

Given this complexity, realistic magneto-hydrodynamic (MHD) simulations have become essential for understanding how stars assemble in such environments and how their feedback modifies the surrounding gas during formation (M. Y. Grudić et al.

2019; C. Federrath & R. S. Klessen 2012; J. E. Dale et al. 2013). However, this realism comes at a high computational cost. It is currently not possible to run sufficiently large suites of state-of-the-art simulations to (i) explore large ensembles across initial conditions and star formation prescriptions, (ii) follow star clusters for significant periods after their formation – when the dynamical consequences of the initial conditions become recognizable – and (iii) disentangle which outcomes are a direct consequence of the star formation process and which arise from the intrinsic stochasticity of stellar dynamics. Many important phenomena are intrinsically rare, such as the production of runaway stars, the detailed kinematics of O and B star populations, or the emergence and survival of sub-clusters in different turbulent realisations (M. S. Fujii & S. P. Zwart 2011; R. Smith et al. 2011; R. J. Parker et al. 2014; J. P. Farias et al. 2015). Robustly characterising such effects therefore requires large sets of statistically equivalent simulations, which remains prohibitively expensive with current computational resources.

At the same time, many of the key observables used to link star formation to present-day stellar populations

are fundamentally dynamical in nature. These include the bound fraction after gas dispersal (S. P. Goodwin & N. Bastian 2006; H. Baumgardt & P. Kroupa 2007), the development of mass segregation and the survival and interacting effects of binaries and higher-order multiples (N. Moeckel & M. R. Bate 2010; R. J. Parker et al. 2011; V. Pavlík 2020). Addressing these questions requires long integrations and controlled ensembles, conditions under which direct N -body methods excel, provided they are supplied with a physically grounded, time-dependent description of the natal environment in which the stars formed.

This is why simplified dynamical models remain essential. They allow rapid, controlled experiments and large ensembles, making it possible to isolate the impact of specific physical ingredients without re-running full MHD each time. The key is to make the simplifications meaningful, retaining the relevant consequences of the underlying physical processes reducing computational cost and unnecessary degrees of freedom, while retaining the overall environment that most strongly conditions the stellar dynamics.

In this paper we introduce the Dynamical Cluster Assembly Framework (D-CAF), implemented within AMUSE (S. Portegies Zwart et al. 2013; F. I. Pelupessy et al. 2013), to model star cluster formation as the gradual assembly of stars within an evolving external potential whose global evolution is motivated by realistic MHD simulations. Our goal is not to reproduce the full hydrodynamics, but to retain the time-dependent environment that matters most for stellar dynamics, enabling systematic and long-term studies that are impractical with full MHD alone.

In this first work we focus on the global evolution of the natal gas in suites of MHD simulations, asking what aspects of that evolution are robust across setups, and what their dynamical consequences are for cluster survival under gas dispersal.

2. METHODS

The goal of this work is to identify the large-scale, time-dependent gas environment in which stars form, and to study how this environment affects the subsequent dynamical evolution of the stellar system. To do this, we analyse MHD star formation simulations, extract the time evolution of the natal gas, and use this information to build dedicated N -body models with time-dependent background potentials.

For this purpose, we developed the Dynamical Cluster Assembly Framework (D-CAF), which separates the problem into two parts. First, we measure the global gas evolution from the MHD simulations. Second, we

evolve the forming stellar population inside that background using direct N -body simulations. This lets us keep the main large-scale effect of the gas while avoiding the computational cost of following the full hydrodynamics. With this approach, we can isolate the effect of the underlying star formation prescription on the long-term stellar dynamics.

2.1. Framework

We built D-CAF inside the AMUSE framework, which we use to couple the different parts of the calculation and to handle the data output. The framework has three main components: i) the N -body integrator, which evolves the stellar orbits, ii) the user-provided star formation scheduler (hereafter framework), which specifies when and how stars are formed, and iii) the time-dependent background potential, which describes the large-scale evolution of the natal gas. These components are modular and can be easily replaced in order to adapt to new setups.

The system can in principle be extended to include additional modules, such as stellar evolution, although we do not include these in this first work. Our goal here is not to build a full-physics simulation, but to isolate the stellar dynamical response to a time-evolving gas background under a controlled star formation prescription. What is considered sufficiently realistic is therefore set by the problem being studied.

We couple the N -body integrator and the background gas using BRIDGE (M. Fujii et al. 2007), as implemented in AMUSE. In this scheme, the stellar system feels the gravitational force of the background potential at fixed coupling intervals. We represent the gas with an analytical model whose evolution can be given either by an explicit functional form or by parameters tabulated in time, in which case we interpolate the potential parameters between outputs.

For the stellar dynamics we use PETAR (L. Wang et al. 2020), a collisional N -body code that combines a fourth-order Hermite scheme for close interactions with a Barnes & Hut tree algorithm (J. Barnes & P. Hut 1986) for long-range forces. PETAR also implements a regularization scheme for close binaries within a user-defined radius r_{bin} (see L. Wang et al. 2020, for details).

We choose the BRIDGE coupling timestep to be no smaller than the internal timestep of the N -body integrator, so that the stellar self-gravity and the external potential follow a consistent temporal ordering. In practice, we set the BRIDGE timestep to an integer multiple of the N -body timestep, with both written as exact powers of two. This choice simplifies the synchronization

between the different parts of the calculation and avoids numerical artefacts from incommensurate timesteps.

2.2. Target MHD simulations

The first step in our problem is to identify the evolving gas environment in which the stars form. In practice, this means following how the gas distribution changes with time in the star-forming region. To do this, we analyse MHD simulations of molecular clouds that include self-gravity and stellar feedback. From these simulations, we extract the time evolution of the gas mass distribution, central concentration, and characteristic spatial scales of the natal environment.

We use star cluster formation simulations produced with two independent frameworks that follow different approaches to star formation: the Star FORMation in Gaseous Environments (STARFORGE) simulations (M. Y. Grudić et al. 2021b; D. Guszejnov et al. 2023) and the TORCH framework (J. E. Wall et al. 2019, 2020). STARFORGE models star formation by resolving individual stars as sink particles that accrete gas self-consistently and includes a broad set of stellar feedback processes. However, STARFORGE uses a non-specialized N -body treatment that does not fully resolve very close encounters and hard binaries. TORCH instead uses a modular framework in which stars form from a predefined list sampled from an initial mass function and are coupled to the gas through sink particles. TORCH includes a more limited set of feedback processes, but it adopts observationally motivated binary populations and uses a dedicated N -body solver that resolves hard binaries and close encounters more accurately. Using both frameworks lets us test which trends are robust across different star formation prescriptions and which depend more strongly on the details of the stellar dynamics. Below, we briefly describe each framework and the specific simulations used in this work.

2.2.1. STARFORGE simulations

The STARFORGE framework is implemented in the MHD code GIZMO (P. F. Hopkins 2015; M. Y. Grudić et al. 2021a). It uses the Lagrangian meshless finite-mass (MFM) method to solve the MHD equations under the ideal MHD approximation (P. F. Hopkins 2015; P. F. Hopkins & M. J. Raives 2016), together with an improved Barnes & Hut algorithm (V. Springel 2005) to compute self-gravity. These simulations resolve the formation of individual stars with sink particles and include the main stellar feedback channels, such as radiation pressure, photoionization, stellar winds, and supernovae (e.g. M. Y. Grudić et al. 2018, 2021b; D. Guszejnov et al. 2021). Gravitational interactions between sink particles

are solved with a fourth-order Hermite integrator. However, unlike PeTar, STARFORGE does not include regularization for close encounters and binaries. It therefore uses a softening radius of 80 AU to avoid prohibitively small timesteps.

We use the fiducial simulation from D. Guszejnov et al. (2022), their M2e4 model which correspond to initially spherical turbulent molecular clouds with mass $2 \times 10^4 M_\odot$ and radii of 10 pc with uniform density. We refer to this run as the `starforge_fiducial` model.

2.2.2. TORCH simulations

TORCH is a modular framework developed in AMUSE that couples the gas and stellar dynamics through BRIDGE (M. Fujii et al. 2007). It evolves the gas with the adaptive mesh refinement MHD solver FLASH (B. Fryxell et al. 2000), while it follows stellar dynamics with the direct N -body solver PeTar. TORCH includes radiative feedback self-consistently through the radiation hydrodynamics module implemented in FLASH, as well as stellar winds and supernova feedback, but it does not include protostellar outflows in the simulations used here.

We focus on the M1 simulation presented in C. Cournoyer-Cloutier et al. (2024), hereafter `torch_M1`. This simulation follows a $2 \times 10^4 M_\odot$ turbulent spherical cloud with a Gaussian initial density profile. The cloud is initialized with supersonic turbulence and then allowed to collapse under self-gravity until feedback regulates further star formation.

As in STARFORGE, TORCH forms stars through sink particles. The main difference is that these sink particles do not represent individual stars. Instead, TORCH forms stars from a predefined list sampled from a P. Kroupa (2002) initial mass function, including the observationally motivated binary prescription introduced by C. Cournoyer-Cloutier et al. (2020).

2.3. Extracting gas evolution from MHD simulations

To build the time-dependent background gas model used in D-CAF, we extract the large-scale gas evolution from the MHD simulations described in §2.2. Our goal is not to reproduce the full gas dynamics, but to capture the time-dependent gravitational environment in which stars form and evolve.

Throughout this work, we define t_0 as the time at which the first star forms. To characterize the part of the gas evolution that is dynamically relevant for the stars, we measure the fraction of gas retained within a fixed set of initial gas Lagrangian radii, F_{ret} , as a function of time. This quantity gives a simple measure of how the gas redistributes during the simulations. The left panels of Figure 1 show the evolution of F_{ret} for

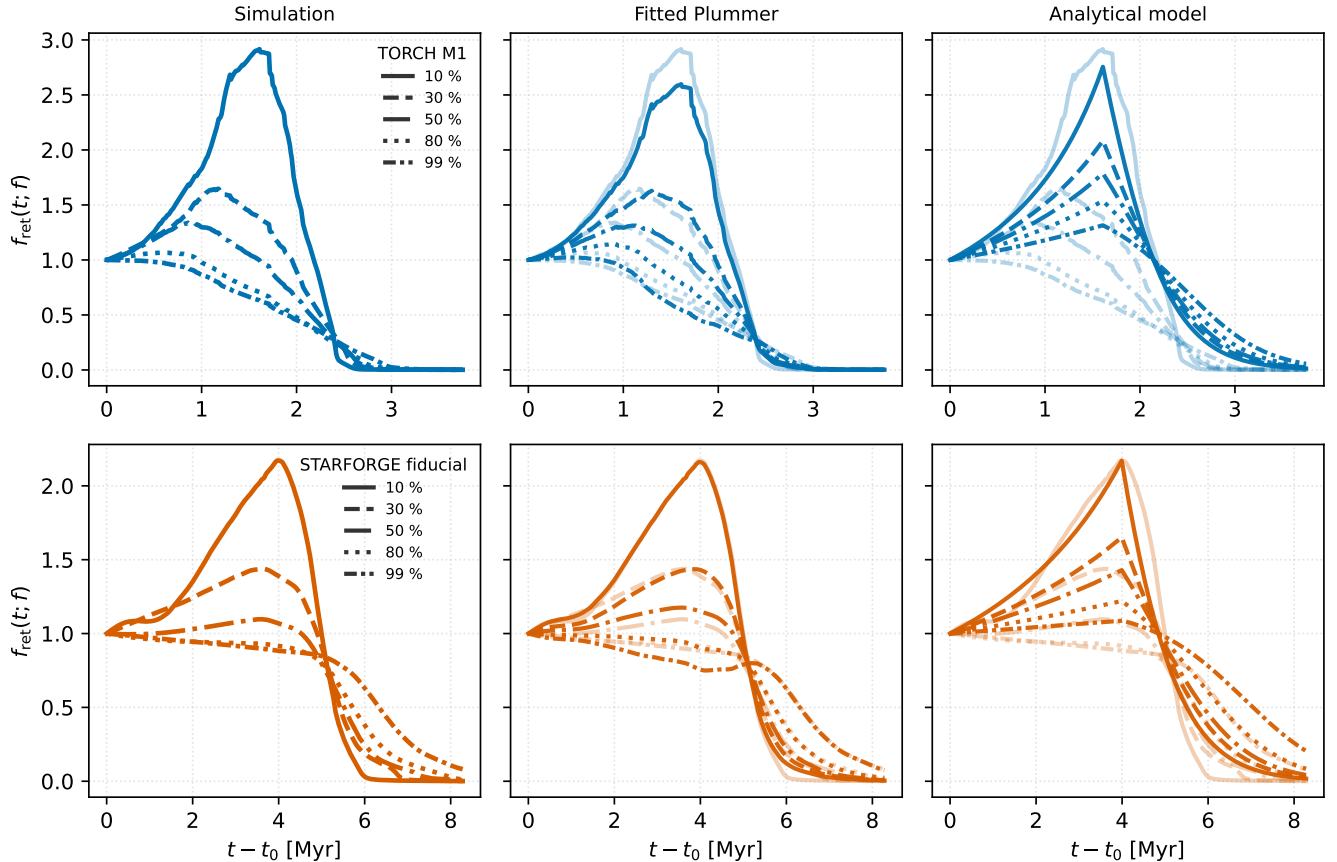


Figure 1. Evolution of the retained gas fraction, $F_{\text{ret}}(t; f)$, measured within fixed initial gas Lagrangian radii for the `torch_M1` (top row) and `starforge_fiducial` (bottom row) simulations. The left panels show the values measured directly from the MHD simulations. The middle panels show the corresponding $F_{\text{ret}}(t)$ reconstructed from the fitted Plummer profiles at each snapshot. The right panels show the analytic model used to parametrize the gas evolution. In the middle and right panels, the fainter lines show the MHD simulation results for comparison.

the MHD simulations considered in this work. The behaviour is broadly consistent with the two-phase picture assumed in classical studies: an embedded phase, during which the gas collapses and becomes more centrally concentrated while stars are forming, followed by a gas-expulsion phase driven by stellar feedback.

For the D-CAF models, we use two different descriptions of this gas evolution. The first uses the measured gas evolution directly through tabulated background potentials, while the second approximates the same evolution using an analytic parameterization. These two approaches are shown in the middle and right panels of Figure 1, and are described below.

To connect this global evolution to the spatial structure of the gas, we also compute radial gas density profiles at each available snapshot, centred on the simulation origin. We average the density in equal-volume shells, which filters out small-scale substructure and anisotropy while retaining the overall radial distribution

of the gas. We use a fixed region of the simulation domain, chosen to contain 90% of the stellar mass at all times.

Figure 2 shows example density profiles for the `starforge_fiducial` and `torch_M1` simulations at different times. At early times, the profile can deviate from a Plummer form in the outer parts of the cloud. However, these regions contain little stellar mass and have little effect on the stellar dynamics. As the simulations evolve, and before the onset of strong feedback, the Plummer fits generally improve.

At later times, stellar feedback pushes the gas into an expanding shell-like configuration that a simple analytic profile cannot reproduce accurately. We still use a Plummer description in this regime because the gas rapidly approaches a low-density background and its contribution to the gravitational potential becomes small. Although the density fits still show deviations from the simulated profiles, the corresponding gravitational po-

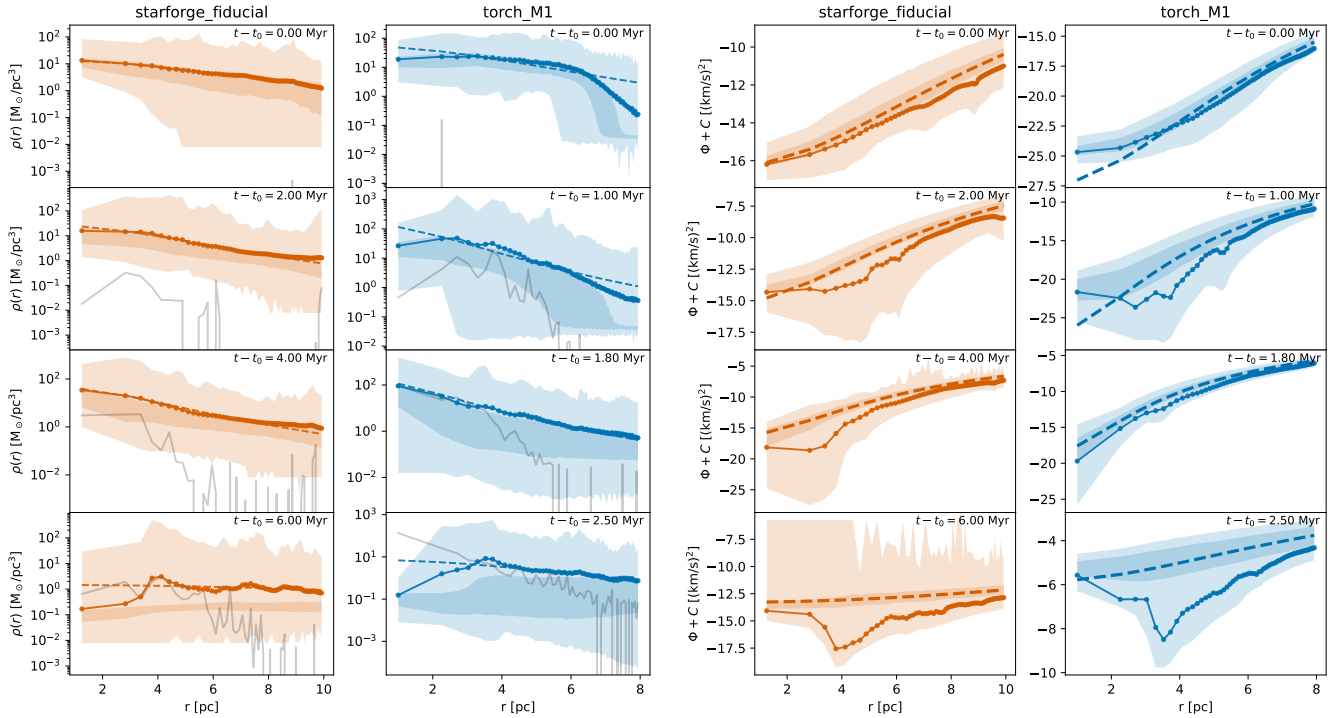


Figure 2. Left: Radial gas and stellar density profiles at different times after the formation of the first star. Circles show the gas density profiles measured in the MHD simulations. Shaded regions indicate the range of values found at each radial shell, with light shading representing the minimum and maximum values and darker shading the 25th and 75th percentiles. Dashed lines show the Plummer models used to characterize the gas distributions. Grey lines show the stellar density profiles for reference. Right: Gravitational potential generated by the gas distribution, measured directly from the MHD simulation outputs. Circles represent the shell-averaged potentials, with shaded regions indicating the minimum, maximum, and interquartile ranges at each radius. Dashed lines show the gravitational potential generated by the fitted Plummer models from the left panel. No fit was performed to the potential itself, apart from an additive constant, since the absolute value of the potential depends on the boundary conditions of the simulations. The potentials generated from the fitted density profiles reproduce the median evolution of the simulated gas potential reasonably well.

tential is reproduced much better. We verified this directly using the potential stored in the simulations. This happens because the potential is a spatial integral of the density field and is therefore less sensitive to small-scale density variations. This is why a spherically symmetric description remains useful even when the density field itself is not well described in detail.

We therefore use the Plummer model to describe the gas structure, given by:

$$\rho(r, t) = \frac{3M_{\text{pl}}(t)}{4\pi R_{\text{pl}}(t)^3} \left(1 + \frac{r^2}{R_{\text{pl}}(t)^2} \right)^{-5/2}, \quad (1)$$

with the Plummer scale radius, R_{pl} , and the Plummer mass, M_{pl} , describing the gas structure at all times. To connect the gas evolution across snapshots, we do not fit each density profile independently. Instead, we fit the evolution of the retained gas fraction, $F_{\text{ret}}(t)$, which more directly captures the redistribution of gas in the region that matters dynamically for the stars. For a given gas mass at each snapshot, matching F_{ret} leaves $R_{\text{pl}}(t)$

as the main parameter controlling the central concentration of the gas. We determine $R_{\text{pl}}(t)$ by minimizing the difference between the measured and modelled F_{ret} , and then determine the corresponding mass normalization across all snapshots. Appendix A describes this fitting procedure in detail.

2.4. Extracting the phase-space properties of stars at formation

The properties of newly formed stars reflect both the local and global conditions of the gas from which they form. However, connecting the gas structure to the stellar phase-space distribution at birth is not simple, since it depends on small-scale substructure, time-dependent accretion, and local feedback. In this work, we therefore use a simpler empirical description of the global stellar phase-space distribution at birth, and leave a more detailed treatment for future work. To do this, we record the positions and velocities of new stars as they first appear in the simulation outputs and use these to build the birth phase-space distributions. This means that

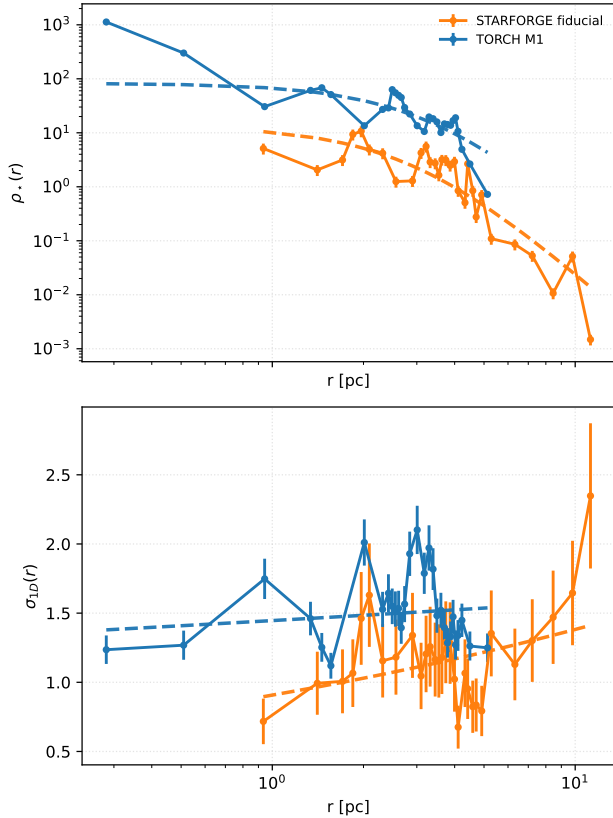


Figure 3. Radial stellar phase-space distributions at the moment stars first appear in the benchmark MHD simulations. Top panel show the stellar density profiles, while the bottom panel show the one-dimensional velocity dispersion profiles. The solid lines show Plummer profile fits to the stellar density and power-law fits to the velocity dispersion profiles used to define the stellar birth prescription adopted in this work.

the extracted birth properties are limited by the time resolution of the simulations.

After collecting these stellar positions and velocities at birth, we construct the radial profiles of each distribution. Figure 3 shows the results for the `starforge_fiducial` and `torch_M1` simulations.

We describe the stellar density profile with a Plummer distribution

$$\rho_*(r) = \frac{3M_*}{4\pi R_{\text{pl},*}^3} \left(1 + \frac{r^2}{R_{\text{pl},*}^2}\right)^{-5/2}, \quad (2)$$

where M_* is the total stellar mass and $R_{\text{pl},*}$ is the stellar scale radius.

We also measure the one-dimensional stellar velocity dispersion as a function of radius. In this work, we use a simple centrally peaked profile and approximate it with

a power law,

$$\sigma_{1D}(r) = \sigma_0 \left(\frac{r}{R_{\text{pl},*}}\right)^{(2-\kappa)/2}, \quad (3)$$

where σ_0 is the velocity dispersion at the reference radius and κ controls the radial slope. We use the same scale radius $R_{\text{pl},*}$ inferred from the stellar density profile to keep the phase-space description consistent. Although the stellar distributions are not truly isotropic nor perfectly described by Plummer spheres, both the density and velocity profiles provide remarkably good first-order fits to the newly formed stellar populations in the benchmark MHD simulations.

In this work, we use these density and velocity dispersion profiles as the stellar birth prescription. They do not attempt to reproduce the full coupling between gas substructure and stellar birth, but rather the first-order phase-space scaling of newly formed stars. The stellar size and velocity scales are normalized relative to the initial gas cloud at the onset of star formation, defining the parameters

$$\eta_r = \frac{R_{\text{pl},*}}{R_{\text{pl,gas}}(t_0)}, \quad (4)$$

and

$$\eta_\sigma = \frac{\sigma_0}{\sqrt{GM_{\text{pl,gas}}(t_0)/R_{\text{pl,gas}}(t_0)}}. \quad (5)$$

For the benchmark simulations analyzed here, the `starforge_fiducial` model gives $\eta_r = 0.44$ and $\eta_\sigma = 0.28$, while the `torch_M1` model gives $\eta_r = 0.55$ and an almost identical velocity scale. We therefore adopt $\eta_r = 0.5$ and $\eta_\sigma = 0.3$ as fiducial values for the model grid, consistent with the approximate scaling found in both benchmark MHD simulations. Since these ratios are inherited from the star formation process, they may depend on the adopted star formation prescription and must therefore be captured at least at this first-order level.

2.5. Star formation prescription

The star formation module, defined by the user, specifies where and how stars form during the simulation. This prescription may or may not be directly linked to the evolution of the background gas. For instance, one may couple the star formation rate to the gas evolution by enforcing a fixed star formation efficiency per free-fall time, ϵ_{ff} , as commonly assumed in analytic and semi-analytic models (J. P. Farias et al. 2019; J. P. Farias & J. C. Tan 2023). However, MHD simulations show that this is not generally the case. Both the global and local star formation efficiencies evolve in a complex manner, and even in isolated simulations we observe continuous

gas infall prior to the onset of feedback, which can temporarily increase the local star formation efficiency.

In this work, we adopt a deliberately simple star formation prescription. We form stars with a fixed phase-space distribution sampled from the empirical relations described in §2.4. This choice avoids introducing additional effects that we aim to isolate in future studies, such as phase-space substructure inherited directly from the gas, which would require a more detailed and consistent mapping from the simulations and is beyond the scope of this first work. We assign stellar masses sampling a P. Kroupa (2002) initial mass function (IMF) between 0.08 and $150 M_{\odot}$, and we do not include primordial binaries. This prescription is intentionally minimal and is designed to ensure that any differences observed in the cluster evolution arise primarily from variations in the background gas potential rather than from the star formation model itself.

2.6. Background gas evolution model

We model the background gas with a time-dependent Plummer sphere. As described in §2.3, we extract this evolution directly from the MHD simulations. At each time, we describe the gas with two quantities: the Plummer mass $M_{\text{pl}}(t)$ and scale radius $R_{\text{pl}}(t)$. We use these in two ways: i) a *tabulated* evolution, taken directly from the MHD simulations and linearly interpolated between outputs (see middle panels of Figure 1), and ii) a parameterized evolution, which we use to explore a wider parameter space (see right panels of Figure 1). Here we describe the parameterized version.

The MHD simulations considered in this work all show the same broad behaviour: an initial contraction phase, during which stars are already forming, followed by a rapid re-expansion once stellar feedback becomes dominant. We therefore model the gas evolution with these two phases.

For $t \leq t_{\text{ge}}$, where $t \leq t_{\text{ge}}$ is the time when gas expulsion begins, we describe the collapse phase with

$$R_{\text{pl}}(t) = R_{\text{pl}0} \left[1 - \frac{t - t_0}{\tau_{\text{col}}} \right]^{1/2}, \quad (6)$$

where $R_{\text{pl}0}$ is the scale radius at $t = t_0$. For the gas mass, we use

$$M_{\text{pl}}(t) = M_0 + \dot{M} (t - t_0), \quad (7)$$

where M_0 is the gas mass at t_0 .

For $t > t_{\text{ge}}$, we describe the gas expulsion phase with

$$R_{\text{pl}}(t) = R_{\text{pl}}(t_{\text{ge}}) \exp\left(\frac{t - t_{\text{ge}}}{\tau_{\text{exp}}}\right), \quad (8)$$

while keeping the gas mass fixed at $M_{\text{pl}}(t_{\text{ge}})$. Here τ_{exp} sets the timescale over which the background potential

disappears after the gas has reached its maximum concentration.

In the runs used in this work, we take $\dot{M} = 0$, so that the mass remains constant and the time dependence enters mainly through $R_{\text{pl}}(t)$. We make this choice because gas accretion from larger scales during the collapse phase makes it difficult to define a unique physically meaningful mass slope within the reference region.

We determine the parameters of this model from the shell-based retention analysis described in §2.3. We use the onset properties to fix $R_{\text{pl}0}$ and M_0 , and we use the peak of the retained gas fraction at the chosen calibration shell to define t_{ge} and the maximum retention factor $F_{\text{ret,max}}$. In this work, we take the calibration shell to be the initial 10% gas Lagrangian radius. For $\dot{M} = 0$, the value of $F_{\text{ret,max}}$ fixes the Plummer radius at the transition time,

$$R_{\text{pl}}(t_{\text{ge}}) = r_{\text{cal}} \sqrt{(f_{\text{cal}} F_{\text{ret,max}})^{-2/3} - 1}, \quad (9)$$

and the collapse timescale then follows from

$$\tau_{\text{col}} = \frac{t_{\text{ge}} - t_0}{1 - (R_{\text{pl}}(t_{\text{ge}})/R_{\text{pl}0})^2}. \quad (10)$$

We then determine the remaining timescale t_{exp} by comparing the post-peak retention tail of the analytic model to the measured retention curves and selecting the value that minimizes the residual. The resulting best-fitting parameters for the benchmark simulations are listed in Table 1, while the corresponding fits are shown in the right panels of Figure 1. Despite the simplicity of this prescription, the parameterized evolution reproduces the global gas evolution of the MHD simulations remarkably well, capturing both the contraction phase and the subsequent gas-expulsion phase with only a small number of parameters.

2.7. N-body star formation simulations

For each target simulation, we run two classes of models. First, we run a *tabulated* model in which the time-dependent Plummer mass $M_{\text{pl}}(t)$ and scale radius $R_{\text{pl}}(t)$ are taken directly from the empirical fits to the MHD simulations and interpolated in time. These runs provide the most direct comparison to the original simulations, since they add no further assumptions about the gas evolution.

Second, we run a family of *parameterized* models in which the background gas follows the analytic description introduced in §2.6. In these runs, we match the same reference radius R_{ref} and enclosed gas mass $M_{\text{gas}}(< R_{\text{ref}}, t_0)$ as in the target simulation at the onset of star formation, while allowing the maximum retained gas fraction $F_{\text{ret,max}}$ to vary. This lets us test

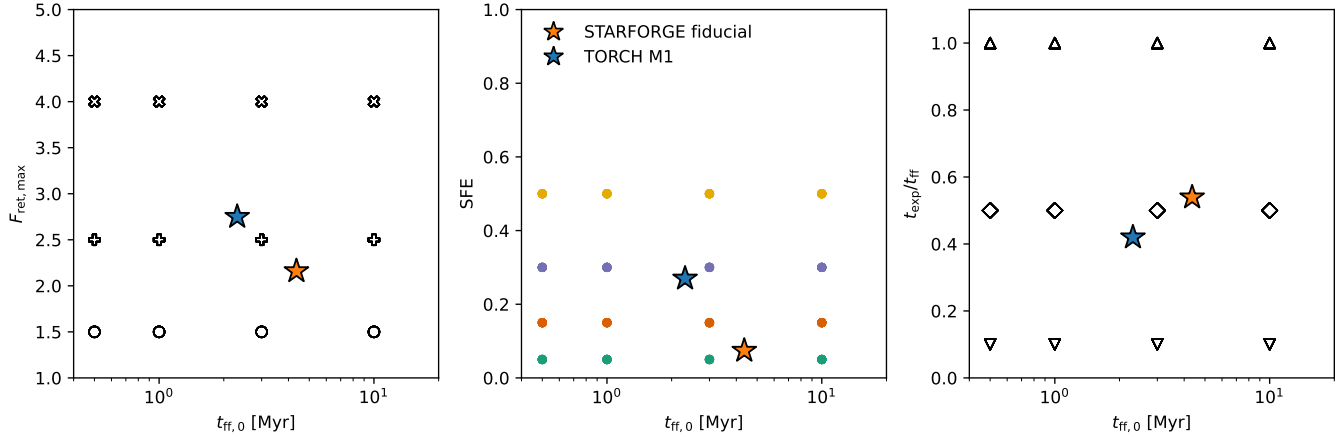


Figure 4. Parameter-space coverage of the simulation suite. Each panel shows the grid (blue circles) explored in this work, with the free-fall time t_{ff} on the horizontal axis. Left: Maximum retained gas fraction $F_{\text{ret,max}}$ versus t_{ff} . Middle: Star formation efficiency (SFE) versus t_{ff} . Right: Gas expulsion timescale normalized by the free-fall time, $t_{\text{exp}}/t_{\text{ff}}$, versus t_{ff} . Starred symbols indicate the reference MHD simulations (STARFORGE and TORCH), placed at their corresponding measured parameter values. The grid represents a controlled experimental design intended to show the baseline roles of gas concentration, star formation efficiency, and gas removal timescale in setting early cluster evolution and stellar kinematics. The same color coding and symbols are used through the paper.

how changes in the maximum gas concentration affect the subsequent stellar dynamics.

For each target simulation, we run multiple realizations with different random seeds. We choose the number of realizations so that the combined stellar population in each parameter set is comparable to the stellar mass formed in the corresponding MHD simulation, while keeping the stellar mass of each individual realization fixed. We do not include primordial binaries or stellar evolution in these runs.

We then extend the analysis beyond the benchmark MHD models by exploring a grid in the main parameters controlling the background gas evolution. Each simulation is defined by the maximum retained gas fraction $F_{\text{ret,max}}$, measured at the initial 10% gas Lagrangian radius, the global star formation efficiency (SFE), the gas-expulsion timescale normalized to the free-fall time $t_{\text{exp}}/t_{\text{ff}}$, and the initial free-fall time t_{ff} , which sets the overall density scale of the system.

Across the grid, we explore different values of $F_{\text{ret,max}}$, SFE, $t_{\text{exp}}/t_{\text{ff}}$, and t_{ff} , extending the ranges covered by the benchmark simulations. We summarize the parameter mapping in Table 2 and show it in Figure 4, together with the location of the reference MHD simulations. With this grid, we aim to isolate how the large-scale evolution of the background potential affects the stellar dynamics across different environments, while keeping the stellar birth prescription fixed.

The reference MHD simulations are not necessarily expected to follow the trends defined by the controlled grid exactly. The grid isolates the effect of the large-

scale evolution of the background potential under spherical symmetry, while the original MHD simulations additionally contain substructure, anisotropic collapse, local non-equilibrium motions, and different treatments of binaries and close encounters. Therefore, deviations between the benchmark MHD models and the controlled grid are expected and provide information on which aspects of the stellar dynamics are driven mainly by the global gas evolution and which depend more strongly on the additional physics present in the full MHD calculations.

3. RESULTS

3.1. Reproducing the MHD gas environment

As discussed in Section 2.3, the Plummer-based reconstruction of the gas distribution reproduces the large-scale gravitational potential of the MHD simulations reasonably well. Since the stellar dynamics are mainly sensitive to the global gravitational field, rather than to the detailed gas density structure, this is a suitable description of the background environment in the present models.

We now examine the resulting dynamical evolution of the stellar systems. As a first step, we compare the target models to the benchmark MHD simulations used to calibrate the gas potential. Figure 5 shows the evolution of the stellar half-mass radius in the original MHD simulations together with the two versions of the target models: the runs using tabulated background gas and the runs using an analytical parameterized gas evolution. In both cases, the stars are formed from the same

Table 1. Benchmark D-CAF models used to reproduce the STARFORGE fiducial and TORCH M1 reference simulations. The tabulated runs use the fitted time-dependent gas evolution extracted directly from the MHD simulations, while the parameterized runs use the corresponding analytic gas model. In both cases, the stellar birth distribution is fixed by the values of η_r and η_σ , which set the scale of the stellar Plummer distribution relative to the initial cloud.

Model	Gas	$F_{\text{ret,max}}$	t_{ge} (Myr)	t_{exp} (Myr)	t_{ff} (Myr)	M_\star (M_\odot)	SFE	$R_{\text{pl},\star}$ (pc)	σ_0 (km s^{-1})	η_r	η_σ	N
SF_fiducial tabulated	table	2.17	–	–	4.45	1023	0.074	2.94	1.11	0.44	0.28	10
SF_fiducial parameterized	analytic	2.16	3.96	2.35	4.45	1023	0.074	2.94	1.11	0.44	0.28	10
TORCH_M1 tabulated	table	2.92	–	–	2.36	6640	0.27	3.42	1.52	0.55	0.28	2
TORCH_M1 parameterized	analytic	2.75	1.60	0.97	2.36	6640	0.27	3.42	1.52	0.55	0.28	2

NOTE— The tabulated $F_{\text{ret,max}}$ values correspond to the measured peak within the 10% reference radii.

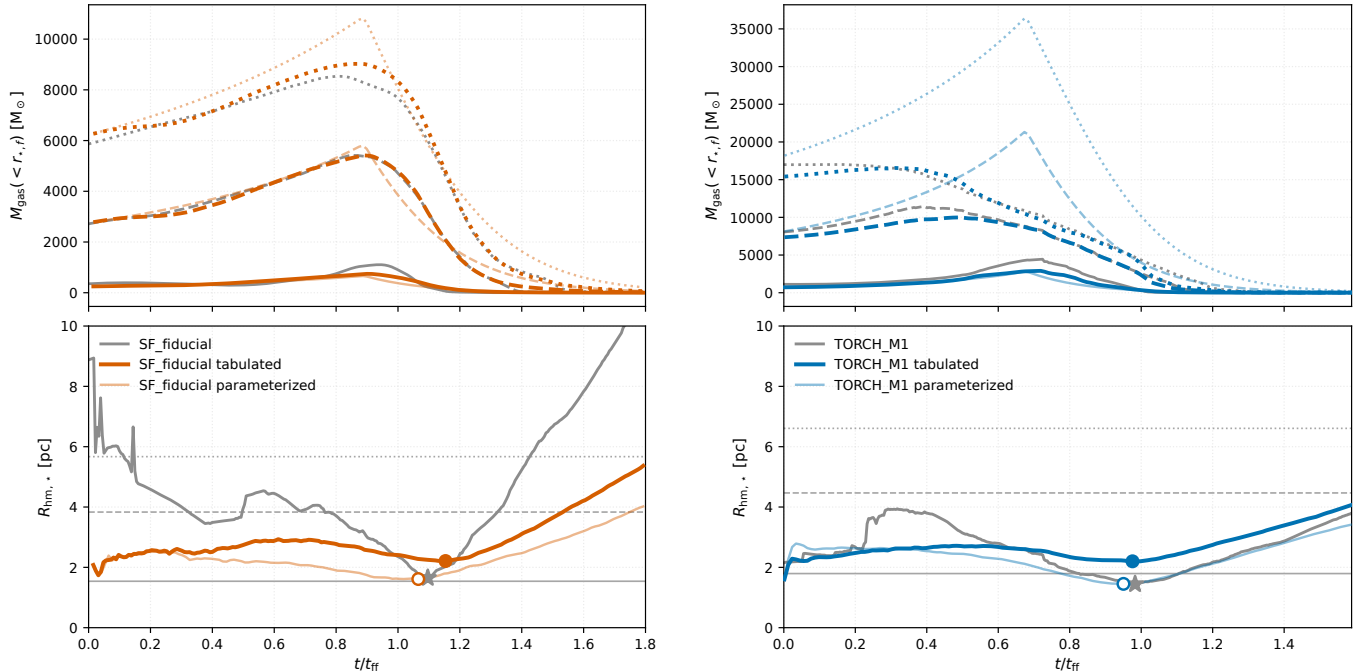


Figure 5. Summary of the target simulations designed to reproduce the background environments of the STARFORGE fiducial model (left) and the TORCH M1 model (right). The bottom panels show the stellar half-mass radius, $R_{\text{hm},\star}$, for the original simulation, a realization using the tabulated Plummer background gas fits directly (tabulated), and a realization using a Plummer sphere with an analytical prescription for its evolution (parameterized). The horizontal lines mark the reference radii containing 10% (solid), 50% (dashed), and 75% (dotted) of the target stellar population, obtained by fitting the positions and velocities of stars at birth in the original simulations (see text). The top panels show the gas mass enclosed within these reference radii. Star symbols highlight the location of the minimum stellar half mass radius of the benchmark MHD simulations, while filled and empty circles shows the same metric for the tabulated and parameterized simulations respectively.

statistical phase-space distribution, obtained by fitting a Plummer profile to the stellar positions and velocities at birth in the MHD simulations, as described in Section 2.4. The top panels show the gas mass enclosed within fixed reference radii defined from the target stellar population, and are therefore the same within each set.

We find that both model realizations reproduce the main contraction of the gas and the corresponding response of the stars. In both the STARFORGE and

TORCH benchmarks, the models reach a similar minimum stellar half-mass radius at approximately the correct time, after which the systems expand as gas removal proceeds. This shows that the simplified background descriptions already capture the main global response of the stellar system.

At the same time, the two implementations do not reproduce the collapse to the same degree. In both benchmark suites, the minimum half-mass radius of the original MHD simulations is more closely reproduced by the

Table 2. Parameter ranges adopted for the D-CAF grid. The grid is defined by fixed stellar masses and by varying the gas-evolution and star-formation parameters over the ranges listed below.

Parameter	Value
M_*	$1000 M_\odot$
SFE	[0.05, 0.15, 0.3, 0.5]
$F_{\text{ret,max}}$	[1.5, 2.5, 4.0]
$t_{\text{ge}}/t_{\text{ff}}$	1.0
$t_{\text{exp}}/t_{\text{ff}}$	[0.1, 0.5, 1.0]
t_{ff}	[0.5, 1.0, 3.0, 10.0] Myr
η_σ	0.3
η_{radius}	0.5
κ	1.8
M_{cl}	M_*/SFE
R_{cl}	$(8GM_{\text{cl}}t_{\text{ff}}^2/\pi^2)^{1/3}$

parameterized runs, while the tabulated models remain systematically less concentrated, despite following the gas evolution more directly. This difference arises because the parameterized models retain a deeper large-scale background potential during the embedded collapse phase. Although the tabulated models can reach comparable or even larger central gas concentrations, the parameterized models retain more gas mass at larger radii during the same period. As a result, the stellar systems evolve inside a globally deeper potential well during the collapse phase, leading to a stronger contraction.

This agreement should, however, be treated with care. The minimum value of $R_{\text{hm},*}$ in the MHD simulations may also reflect the intrinsic phase-space substructure of the newly formed stars, which is deliberately not included in the present idealized models. For this reason, the closer match between the parameterized runs and the MHD benchmarks may be partly coincidental. In that sense, the difference between the tabulated and parameterized values of $R_{\text{min},*}$ is more useful as an estimate of how sensitive the stellar collapse is to small variations in the background gas description. The main point is therefore not that one realization reproduces the benchmark minimum exactly, but that the large-scale gas evolution already places a strong constraint on the stellar concentration, and that modest differences in the gas model can still produce noticeable differences in the depth of the collapse.

The differences between the benchmark simulations and the target models are already informative. In the `starforge_fiducial` case, the original simulation shows a faster post-gas-expulsion expansion than either of the corresponding models. By contrast, the expansion of the `torch_M1` case is more closely reproduced by the

target simulations. This difference is already visible during the collapse phase. The `starforge_fiducial` simulation shows a larger half-mass radius at early times, significantly larger than in the simplified models, despite having the same statistical phase-space distribution at birth. This is consistent with earlier star formation occurring farther from the centre of the potential well, which leads to a stronger subsequent collapse and, once the gas is removed, to a faster expansion. By contrast, the `torch_M1` simulation appears to follow a stellar assembly history closer to the description adopted in the present models, which may explain the better agreement during the expansion phase. This suggests that the radial profile alone does not provide a complete description of the star formation process. Phase-space correlations, substructure, and assembly history can also be important ingredients of the stellar birth prescription.

Even so, the comparison shows that the present models capture the main response of the benchmark simulations. This gives us a baseline for how an idealized star formation prescription reacts to a more realistic background gas evolution than is usually included in N -body models. The point of this baseline is not to reproduce all aspects of the original MHD simulations, but to isolate the effect of the large-scale gas environment on the early structural evolution of the stellar system. With this reference in place, we can now examine how the same baseline responds across the broader parameter space explored by the model grid.

3.2. Simulations grid

We now extend the baseline established in the previous section to the wider parameter space described in Table 2. The goal of this simulation grid is to explore how stars formed under the same idealized star formation prescription respond to different background environments, while keeping the total stellar mass fixed at $1000 M_\odot$.

Figure 6 shows the evolution of the stellar half-mass radius, R_{h} , across the simulation grid, grouped by SFE, which sets the depth of the gas potential relative to the stellar mass, and by t_{ff} , which sets the density scale of the natal environment. While the trends in these models will be quantified in the following sections, the figure already provides a global view of the behaviour of the simulations across the grid. The overall evolution mirrors the benchmark simulations: an embedded phase during which the stars form and contract, followed by an expansion phase as gas removal weakens the background potential. Within this common sequence, $F_{\text{ret,max}}$ mainly modulates the depth of the contraction, while the nor-

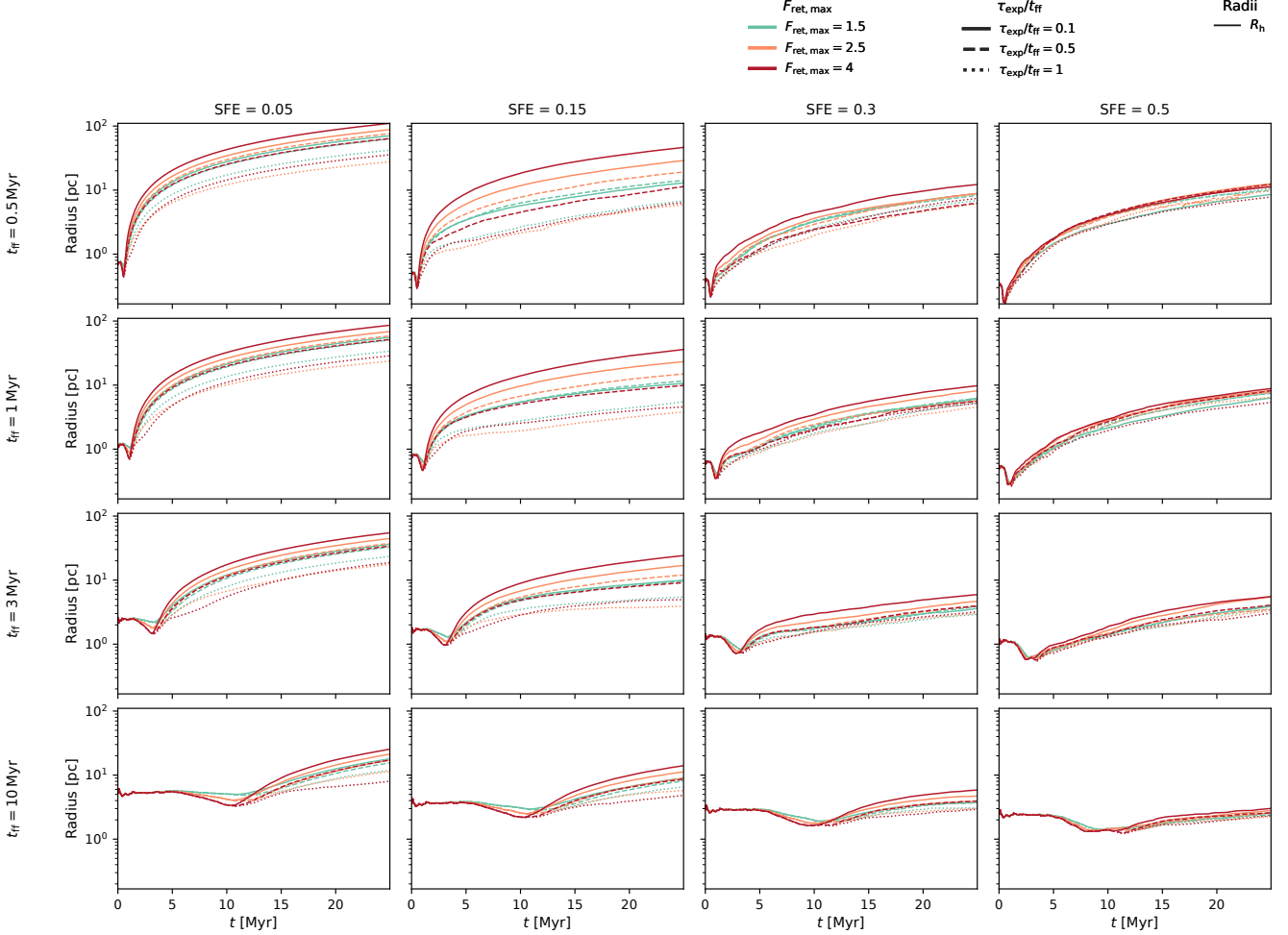


Figure 6. Evolution of the stellar half-mass radius, R_h , across the simulation grid. Columns show different free-fall times, while rows correspond to different SFE values. Colours indicate the maximum retained gas fraction, $F_{\text{ret,max}}$, and line styles indicate the gas-expulsion timescale. The overall evolution follows a common sequence across the grid: an embedded contraction phase while the gas collapses and stars form, followed by expansion after gas removal weakens the background potential. Lower-SFE systems and shorter free-fall times produce the largest dynamical range in size, reaching both deeper contraction and stronger subsequent expansion. Increasing $F_{\text{ret,max}}$ mainly deepens the contraction, while longer gas-expulsion timescales preserve more compact stellar systems after gas removal.

malized gas-expulsion timescale, $\tau_{\text{exp}}/t_{\text{ff}}$, controls how abruptly the systems enter the expansion phase.

A clear scale contrast is visible across the grid and appears to be mainly set by t_{ff} . Shorter t_{ff} leads to systems with a much larger dynamical range in size within the first 25 Myr, reaching both deeper contraction and stronger subsequent re-expansion. This behaviour is particularly strong in the low-SFE models. By contrast, larger t_{ff} leads to a weaker structural response and more stable stellar systems. At fixed t_{ff} , increasing SFE gener-

ally helps preserve more compact systems after gas expulsion, while longer gas-expulsion timescales strongly suppress the later expansion.

Overall, the grid already shows that the global structural evolution is mainly modulated by t_{ff} and SFE, while $F_{\text{ret,max}}$ and the gas-expulsion timescale shape the strength of the contraction and expansion phases. However, the stellar population does not respond to gas removal on the initial cloud free-fall timescale, but on its own dynamical timescale reached at the onset of

gas expulsion. As the gas contracts during the embedded phase, the stellar velocity dispersion increases and the stellar crossing time decreases. Therefore, the same physical gas-expulsion timescale can correspond to very different effective dynamical regimes depending on the embedded evolution reached by the system. We now quantify these dependencies directly through the expansion rates.

3.3. Quantifying expansion rates

A direct consequence of the embedded evolution described above is that the stellar systems tend to expand after gas expulsion. However, the expansion rate is not determined by the imposed gas-expulsion timescale alone, but also by the stellar dynamical state reached before gas removal and by the fraction of the stellar population that remains bound. Systems with more gas contraction develop larger stellar velocity dispersions and shorter crossing times prior to gas expulsion, while the SFE regulates how strongly the gravitational potential changes once the gas is removed. Both effects determine how efficiently the embedded velocity scale is transformed into bulk expansion. This makes the expansion rate a useful quantity to compare across the full simulation grid.

We characterize the expansion using the evolution of the stellar half-mass radius, R_h . After gas expulsion, some systems may still contract for a short time while they relax, but they eventually enter an expansion phase at a rate that depends on the model parameters. We therefore fit a straight line to the time evolution of R_h and define the slope of that fit as the characteristic expansion rate, dR_h/dt , of the simulation. For cleanly expanding systems this relation is close to linear, while in systems retaining a larger bound fraction the evolution of R_h is noisier and less regular. Even in these cases, however, the overall evolution can still be described by a mean expansion rate. In this sense, dR_h/dt should be understood as a global measure of expansion rather than as an instantaneous quantity. The top panels of Figure 7 show the recovered values of dR_h/dt across the model grid. Lower-SFE systems with rapid gas expulsion show the largest expansion rates, reaching values of up to $\sim 3.5 \text{ km s}^{-1}$.

As the SFE increases, the expansion weakens, becoming close to zero for $\text{SFE} = 0.5$. The models separate into three regimes based on the gas-expulsion timescale. In the impulsive case, expansion is strongest, and the systems with the largest $F_{\text{ret,max}}$ also reach the largest values of dR_h/dt . In this regime, the dependence on $F_{\text{ret,max}}$ is clearly visible. When the gas-expulsion timescale increases to half a free-fall time,

which is closer to the timescales measured in the benchmark MHD cases, the dependence on $F_{\text{ret,max}}$ becomes significantly weaker, while SFE still regulates the overall strength of the expansion. In practice, in this regime only the lowest-SFE systems show substantial expansion, while most models with $\text{SFE} \geq 0.15$ remain below 1.5 km s^{-1} .

This transition becomes clearer when the gas-expulsion timescale is normalized by the stellar crossing time at the onset of gas expulsion, $t_{\text{exp}}/t_{\text{cross}}$. Systems reaching stronger embedded contraction develop shorter crossing times before gas removal, moving the same physical gas-expulsion timescale toward a more adiabatic stellar response. As a result, part of the scatter between different contraction levels decreases when expressed in terms of $t_{\text{exp}}/t_{\text{cross}}$, suggesting that the stellar response is mainly regulated by the local stellar dynamical timescale rather than by the initial cloud free-fall time alone. Remarkably, $t_{\text{exp}}/t_{\text{cross}} \sim 1$ appears to mark the transition between an impulsive regime, where the expansion is regulated mainly by the SFE, and a regime where the gas-expulsion timescale begins to strongly damp the expansion efficiency.

Additionally, the benchmark MHD models provide some insight into the limitations of the simplified spherical framework. For instance, the STARFORGE models tend to reach somewhat larger expansion rates than expected from their measured $F_{\text{ret,max}}$. This extra expansion may be related to how the stellar population assembles in the STARFORGE case. As shown in Fig. 5, the stellar half-mass radius starts larger and contracts strongly, in contrast to the TORCH case, where the half-mass radius is more stable and the collapse is milder. Therefore, when gas expulsion begins in the STARFORGE case, part of the stellar population may still be falling through a potential well that is already weakening. The larger expansion rate may then reflect not only the velocity dispersion reached during formation, but also the coherent radial structure of the velocity field. This suggests that the expansion is affected not only by the amplitude of the embedded kinematics, but also by the assembly history and phase-space coherence of the stellar population.

3.4. Expansion rate observables

While the gas-expulsion timescale regulates how much expansion is produced, the SFE is not by itself the quantity that sets the expansion speed. Instead, the expansion can only draw from the velocity scale already present in the stellar system when gas expulsion begins. In the models presented here, that scale represents the maximum stellar velocity dispersion reached before ex-

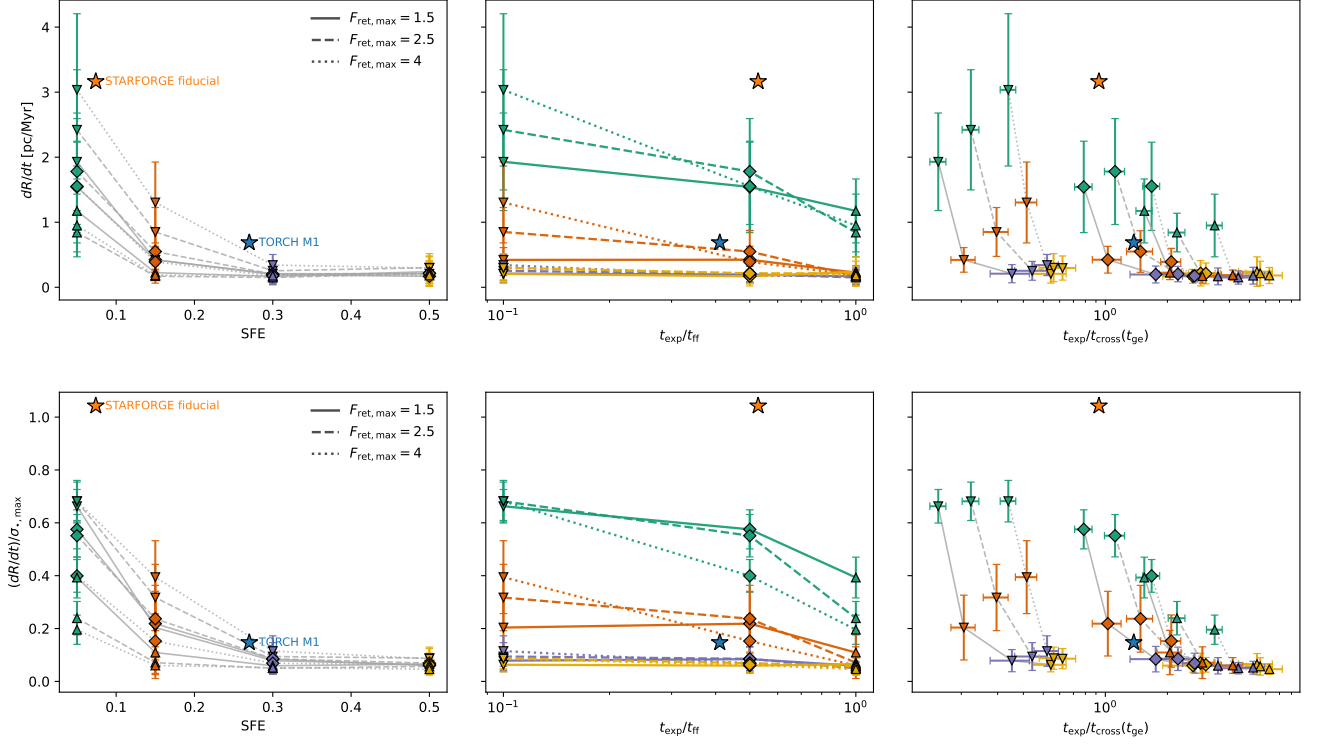


Figure 7. Expansion rates measured at 25 Myr across the full parameter grid. The top row shows the expansion rate of the half-mass radius, dR_h/dt , while the bottom row shows the expansion efficiency relative to the maximum embedded velocity dispersion, $dR_h/dt/\sigma_{*,\max}$. The left column shows the dependence on the nominal SFE, the middle column the imposed gas-expulsion timescale $t_{\text{exp}}/t_{\text{ff}}$, and the right column the effective gas-expulsion timescale measured relative to the stellar crossing time at the onset of gas expulsion, $t_{\text{exp}}/t_{\text{cross}}$. Colors and symbols follow Fig. 4, with colors coding the SFE, symbols the gas expulsion timescale, and lines connecting families with the same $F_{\text{ret,max}}$. Filled stars show the location of the reference MHD models. The maximum expansion rate reached by a system is set by the embedded velocity dispersion before gas expulsion, while the gas-expulsion timescale regulates how efficiently this velocity scale is transformed into bulk expansion. The dependence on gas-expulsion timescale becomes significantly weaker when $t_{\text{exp}}/t_{\text{cross}} > 1$.

pansion, $\sigma_{*,\max}$. The bottom panels of Figure 7 show the expansion rate normalized by this quantity. In the most impulsive cases, the ratio $dR_h/dt/\sigma_{*,\max}$ reaches values of about 0.7, while it decreases rapidly as either the SFE increases or the gas-expulsion timescale becomes longer. This shows that $dR_h/dt/\sigma_{*,\max}$ is better interpreted as a measure of how efficiently the natal velocity scale is converted into bulk expansion, rather than as a direct proxy for the natal velocity scale itself. In this sense, the observed expansion rate provides at best a lower limit on the velocity scale with which the system emerged from its embedded phase.

Since the advent of Gaia, several studies have measured signatures of expansion in young clusters and associations (M. A. Kuhn et al. 2019; N. J. Wright 2018; A. L. Quintana et al. 2025; A. D. Croce et al. 2023). These quantities have generally been used as indicators of expansion, but their relation to the true bulk expansion speed of a stellar system is still not well established. Here we use our homogeneous simulation grid, built from

star-formation models, to compare these commonly used observables directly to the measured expansion of the systems.

We consider three metrics commonly used in the literature. The first is the mean outward velocity of the stars, v_R , which has been used as a direct measure of expansion velocity (e.g. J. J. Armstrong & J. C. Tan 2026). The second is the ratio between outward velocity and radial velocity dispersion, $v_R/\sigma(v_r)$ (e.g. A. D. Croce et al. 2023). Unlike v_R , this quantity does not measure the expansion speed directly, but instead traces how strongly the stellar velocity field is dominated by coherent outward motion relative to random motions. The third metric is the velocity gradient, κ , which is usually measured under the assumption of a single-point expansion pattern and often interpreted as an expansion timescale. The difficulty with κ is that it is not time-invariant: in an unbound and isolated expanding system, stellar velocities remain approximately constant while stellar positions continue to increase, so κ changes

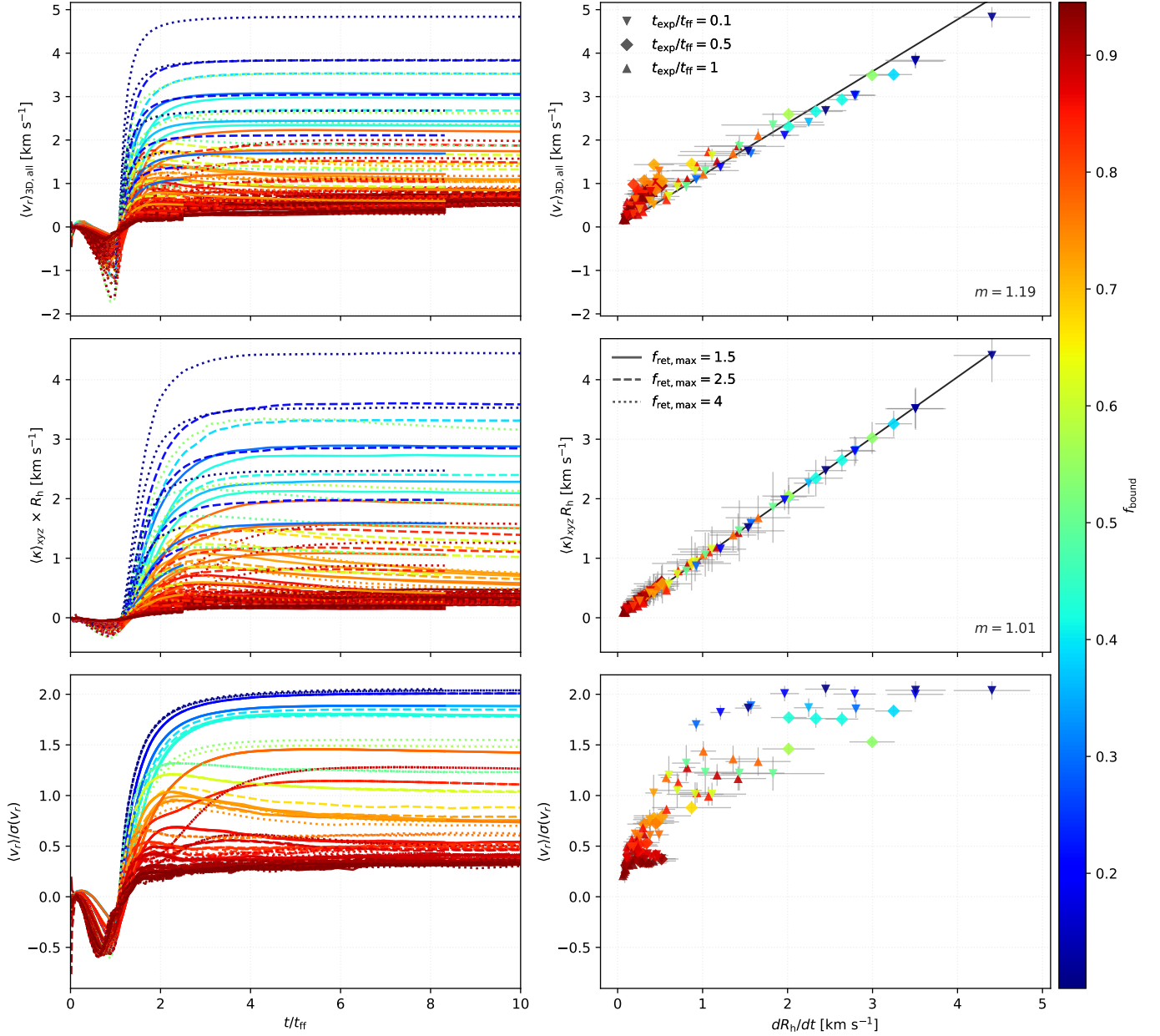


Figure 8. Evolution and interpretation of three observational expansion diagnostics: the average outward velocity, v_R (top panels), the position–velocity expansion gradient, κ multiplied by the current R_h (middle panels), and the ratio between outward velocity and radial velocity dispersion, $v_R/\sigma(v_r)$ (bottom panels). The first two quantities directly measure the physical expansion rate of the stellar population, while $v_R/\sigma(v_r)$ traces how strongly the velocity field is dominated by coherent outward motion. The right panels show the evolution of the metrics as a function of free-fall time, with lines colored by the bound fraction measured $2t_{\text{ff}}$ after gas expulsion. The left panels compare the metrics measured at 25 Myr against the true expansion rate of R_h , with points using the same color scale. Each line and point is an average of 10 simulations with the same properties, with error bars showing the standard deviation of the group. Symbols denote the gas-expulsion timescale following the same coding as Figure 4, while line styles code the central concentration $F_{\text{ret,max}}$. After the systems relax, strongly unbound systems evolve toward more stable values of these metrics, while systems retaining larger bound fractions show continued evolution and larger scatter.

with time even when the expansion speed does not. On its own, κ is therefore difficult to compare across systems. Here we instead multiply κ by a consistent size scale, the half-mass radius, so that it is recast from an inverse timescale into a velocity-like quantity.

Figure 8 shows the evolution of the three metrics across the simulation grid. We normalize time by the corresponding t_{ff} . After gas expulsion, all metrics typically require about two t_{ff} to settle into a roughly constant value. The main exceptions are systems with high bound fractions ($\gtrsim 50\%$), where continued internal evolution breaks the free expansion picture expected for stellar associations.

If we compare v_{R} and κR_{h} to the true bulk expansion of the systems, shown in the right panels of Figure 8, both follow the expansion of the half-mass radius remarkably well. In the case of v_{R} , the mean outward velocity naturally traces the expansion of the stellar distribution. In the case of κR_{h} , the agreement follows from using R_{h} itself as the size scale that converts κ into a velocity. We have verified that this relation is not generally 1:1 for other Lagrangian radii, where an additional calibration is required.

The behaviour of $v_{\text{R}}/\sigma(v_r)$ is qualitatively different. Rather than tracing the physical expansion rate directly, this quantity measures how clean the expansion is relative to the internal velocity dispersion of the system. Strongly unbound systems evolve toward large and approximately constant values of $v_{\text{R}}/\sigma(v_r)$, while systems retaining larger bound fractions continue to evolve and show substantially larger scatter. This suggests that $v_{\text{R}}/\sigma(v_r)$ may provide a useful observational indicator of whether a stellar population is undergoing clean free expansion or still retains a significant bound component. Interestingly, both the simulations and the Gaia cluster sample analyzed by [A. D. Croce et al. \(2023\)](#) span a similar range of $v_{\text{R}}/\sigma(v_r)$ values at early times, with the distributions appearing to saturate around values of ~ 2 .

At the same time, applying these relations to observed systems requires a reliable census of the stellar population, both to estimate R_{h} and to measure v_{R} robustly. In older systems, the outer high-velocity envelope may already be poorly sampled or no longer identifiable in membership surveys, biasing both v_{R} and R_{h} toward lower values. This effect may become particularly important once the expanding stellar population becomes spatially extended and difficult to separate from the Galactic field.

Nevertheless, the relations shown in Figure 8 are promising. They still need to be tested against observational biases and physical effects not included here, such

as anisotropy, primordial binaries, and the Galactic environment. Still, if these metrics trace the true expansion rate of stellar systems, they open the possibility of connecting present-day expansion directly to the embedded velocity scale established during the formation process.

3.5. Amplification of stellar kinematics during formation

As we show in the previous section, the expansion rates are set by the velocity dispersion reached during the formation phase. It is therefore important to understand what drives this velocity scale, and how it depends on the details of the star formation process. Here we examine how this scale is produced across the grid. Figure 9 shows the maximum velocity dispersion and density reached within R_{h} , both normalized to their initial values. This normalization allows us to compare systems with different initial density and velocity scales on an equal ground, isolating the effect of the formation process itself.

On the grid of simulations presented here, stars are formed sampling from a fixed distribution (see §2.5), where the spatial and velocity scales are set by the parameters η_r and η_σ , and tied to the background gas potential. This allows us to define consistent reference scales σ_\star and n_\star for each model. We take σ_\star from the velocity normalization, $\sigma_\star = \eta_\sigma \sqrt{GM_{\text{pl}}/R_{\text{pl}}}$, and define the characteristic stellar density as the mean density within the half-mass radius,

$$n_\star = \frac{3}{8\pi} \frac{N_{\star, \text{final}}}{R_{\text{pl}}^3}, \quad (11)$$

where the numerical factors account for the relation $R_{\text{h}} \approx 1.3 R_{\text{pl}}$ and the use of half the stellar population.

With this normalization, we find that both $F_{\text{ret}, \text{max}}$ and the SFE systematically increase $\sigma_{\star, \text{max}}$ and $n_{\star, \text{max}}$. The dependence on SFE can be understood from the way the stellar distribution is initialized relative to the gas potential. At fixed η_σ and η_r , the stellar size and velocity scales are set as fixed fractions of the background gas potential. As a result, changing the SFE modifies the depth of the potential in which the stars are embedded without changing their relative scaling to it.

Since the stellar mass is fixed across the grid, lower-SFE systems correspond to a more massive gas background, and therefore to a deeper potential. The stellar velocity dispersion then increases accordingly, while the stellar self-gravity remains unchanged. This produces a systematic variation in the dynamical state of the stellar component, such that lower-SFE systems are born dynamically hotter, while higher-SFE systems are closer to equilibrium and can collapse more efficiently prior

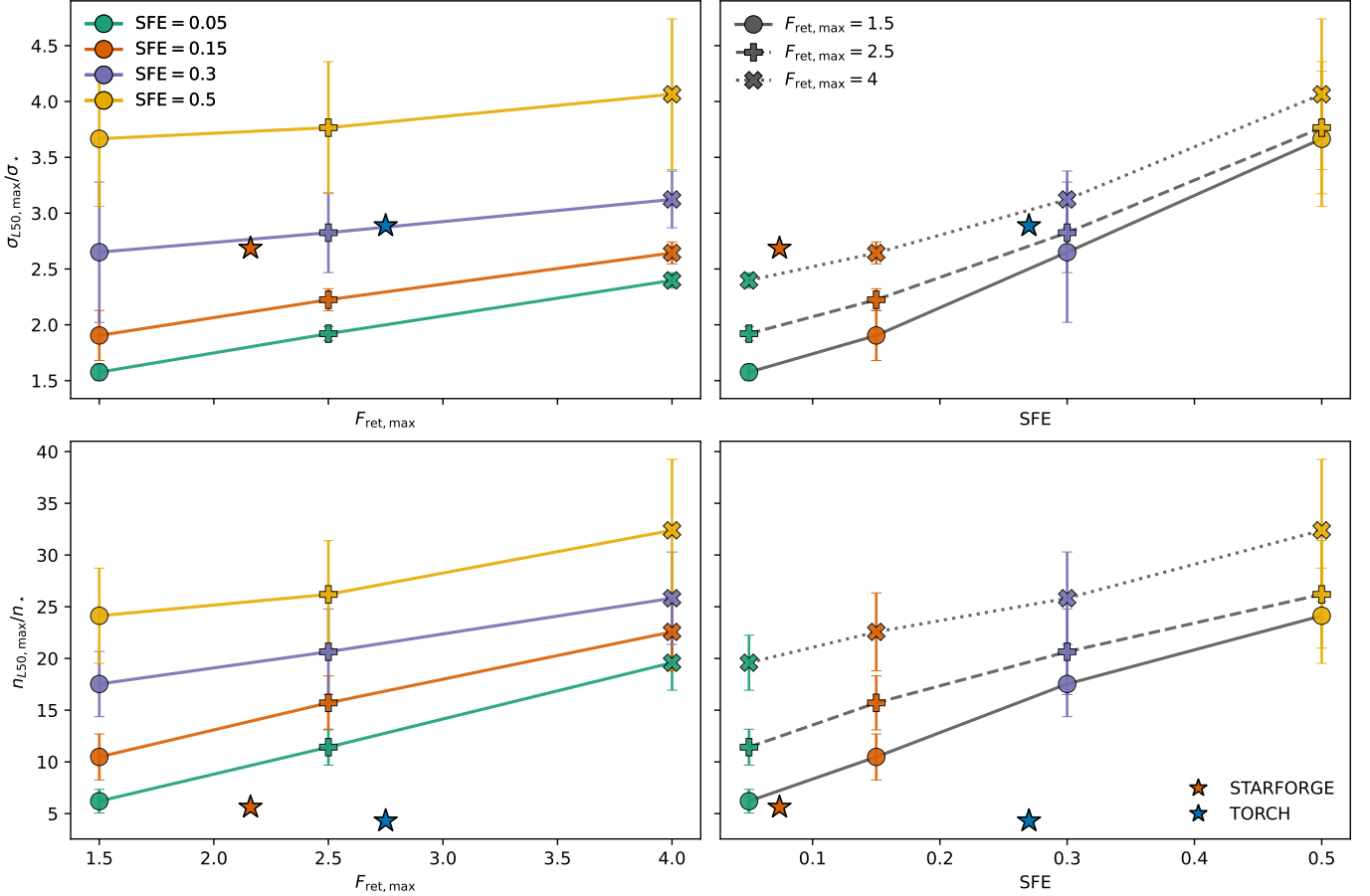


Figure 9. Normalized maximum stellar velocity dispersion and maximum half-mass number density for stars within R_h . The left panels show these quantities as a function of $F_{\text{ret,max}}$, while the right panels show the same measurements as a function of SFE. In all panels, colors indicate SFE and line styles/markers indicate $F_{\text{ret,max}}$. The normalization factors σ_* and n_* are the characteristic formation scales defined from the sampled initial distribution.

to gas expulsion, reaching higher densities and velocity dispersions.

This behaviour follows directly from the way stars are formed in the underlying MHD simulations. In that case, the stellar distribution inherits its size and kinematic scales from the local gas potential at the time of formation, rather than from the self-gravity of the stellar component alone. The parameters η_σ and η_r therefore encode this coupling between stars and gas, and the resulting dependence on SFE reflects the dynamical state in which the stars are assembled. These trends highlight the subtleties of the dynamical formation process imprinted on the resulting stellar population, which are often not captured by MHD simulations alone.

On top of this trend, the evolution of the gas potential modulates the degree of contraction in a more direct way. Increasing $F_{\text{ret,max}}$ leads to a more centrally concentrated gas distribution, deepening the potential felt by the stars and driving an additional increase in both

the velocity dispersion and the stellar density before gas removal.

Figure 9 shows that the amplification of the velocity dispersion is moderate across the grid, ranging between factors of ~ 1.5 to 4 relative to the intrinsic values from the star formation prescription. In contrast, the corresponding increase in $n_{*,\text{max}}$ is significantly stronger, reaching factors of ~ 5 to 30 above the formation values. At fixed $F_{\text{ret,max}}$, increasing the SFE produces the largest change in both quantities, while variations in $F_{\text{ret,max}}$ at fixed SFE lead to more moderate changes in $\sigma_{*,\text{max}}$ and a stronger response in $n_{*,\text{max}}$, particularly at low SFE. Across the full range of SFE, $F_{\text{ret,max}}$ increases the central density by an average factor of ~ 2 between $1.5 < F_{\text{ret,max}} < 4$, and a milder average factor of ~ 1.3 in the velocity dispersion. In both cases, low-SFE systems show the strongest dependence.

The benchmark MHD models do not follow the density trends to the same degree as the velocity amplification. In particular, the TORCH models reach much

lower density concentrations than expected from their measured $F_{\text{ret,max}}$ despite reproducing the velocity amplification more closely. This suggests that the global depth of the potential is reasonably captured by the simplified framework, while the spatial concentration of the stellar population is more sensitive to the detailed assembly process. In particular, the TORCH stellar distribution remains significantly more structured than a smooth Plummer profile, such that global density measures based on the half-mass radius may underestimate the density reached in local collapsing regions. Consistently, using a local-density estimator substantially increases the measured density concentration in the TORCH case, although we leave a systematic comparison between global and local density estimators for future work.

Considering that we explore here only a relatively narrow range of $F_{\text{ret,max}}$ around the values found in the MHD simulations analyzed, the central concentration of gas already plays a significant role in increasing the central concentration of stars. In addition, the relative scaling of the newborn stellar population with respect to the gas is an important factor that sets the velocity scale of the final stellar system, with direct implications for how fast these systems will expand. It remains to be explored with a broader set of MHD simulations how these factors vary across different star formation prescriptions. We note, however, that in other MHD simulations not included here, $F_{\text{ret,max}}$ can reach higher values. Here we have just explored the consequences of such increase, however the conditions that lead to different $F_{\text{ret,max}}$ values and the ranges that are physically possible is a matter that has not yet been explored.

3.6. Bound fraction across the grid

The gas expulsion phase is a crucial stage in the evolution of young star clusters, and as MHD simulations increase in complexity it becomes important to identify the physical quantities that determine whether stellar systems survive gas removal. Classical studies have shown that the survival of young star clusters depends primarily on the SFE and the gas-expulsion timescale. A high SFE leaves enough stellar mass to retain the gravitational potential once the gas is removed, while slow gas removal gives stars time to adapt to the evolving potential. On the other hand, rapid gas expulsion leaves many stars unbound (C. J. Lada et al. 1984; S. P. Goodwin & N. Bastian 2006; H. Baumgardt & P. Kroupa 2007). Other factors are also known to affect cluster survival, such as substructure, which can locally raise the stellar density (R. Smith et al. 2011; J. P. Farias et al. 2015), and the dynamical state of the stars at the

time of gas expulsion, with sub-virial systems generally more likely to survive rapid gas loss (P. L. Lee & S. P. Goodwin 2016; J. P. Farias et al. 2018).

MHD simulations provide important information on how these different processes compete during the formation phase. In this first work, we isolate the two main processes explored in classical studies, the SFE and the gas-expulsion timescale. However, unlike classical idealized models, the gas distribution contracts while stars are forming and the stellar population is not initially in equilibrium. As a result, the embedded phase not only changes the stellar fraction that reaches the center before gas expulsion, but also the stellar dynamical timescale itself. Systems reaching stronger contraction develop both larger stellar velocity dispersions and shorter stellar crossing times before gas removal. Therefore, the response of the stellar population depends not only on the imposed gas-expulsion timescale, but on how this timescale compares to the local stellar dynamical time reached during the embedded evolution.

This is where the initial stellar kinematics become important. Systems formed with colder stellar velocities collapse more efficiently toward the center, raising the local stellar fraction prior to gas expulsion. In contrast, hotter systems are less able to follow the contraction of the gas potential, leading to lower central stellar concentrations and therefore lower bound fractions after gas removal. Therefore, the relevant quantity for cluster survival is not necessarily the global SFE alone, but the local stellar fraction established during the formation phase. The middle row of Figure 10 shows the bound fraction measured $2t_{\text{ff}}$ after gas expulsion as a function of the nominal SFE for two gas-expulsion timescales.

We recover the classical behaviour where larger SFE and slower gas removal lead to larger bound fractions. In the impulsive gas-expulsion regime, $t_{\text{exp}}/t_{\text{ff}} = 0.1$, the bound fraction increases steeply with SFE, with low-SFE systems becoming largely unbound and higher-SFE systems retaining a significant bound component. However, at fixed nominal SFE, the models follow different trends as a function of $F_{\text{ret,max}}$. Systems with larger $F_{\text{ret,max}}$ follow lower bound fractions trends across the SFE.

As shown in the previous section, increasing $F_{\text{ret,max}}$ raises both the stellar density and the velocity scale reached during formation. In the impulsive gas-expulsion regime, the increase in velocity dispersion dominates the response of the system after gas removal, producing dynamically hotter stellar populations that are more easily disrupted. At the same time, the contraction of the stellar distribution also modifies the stellar fraction that reaches the center prior to gas expul-

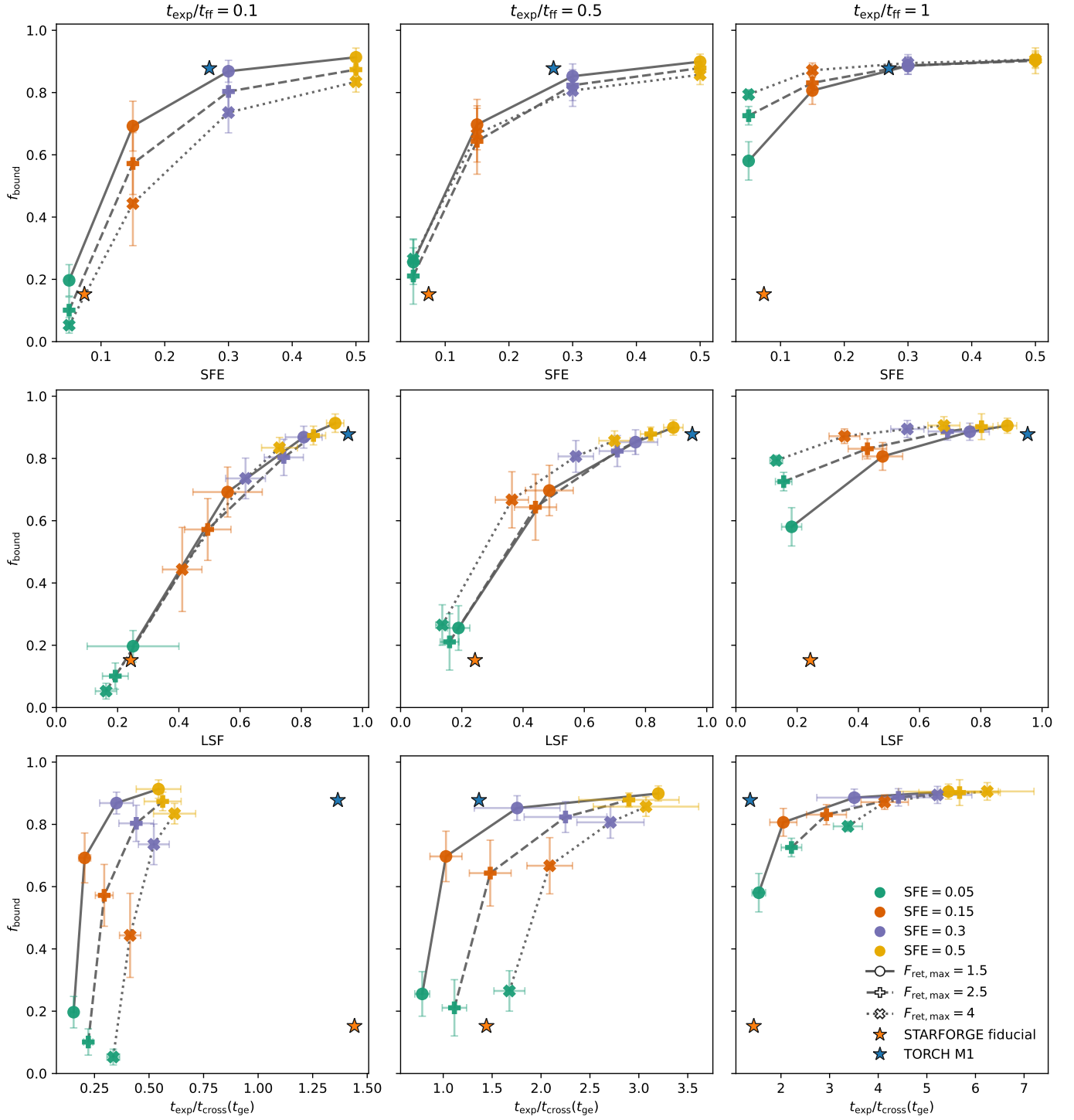


Figure 10. Bound fraction measured at $t_{\text{ge}} + 2t_{\text{ff}}$ across the simulation grid. Columns show the three imposed gas-expulsion timescales, $t_{\text{exp}}/t_{\text{ff}} = 0.1, 0.5,$ and 1 , from left to right. The top row shows the bound fraction as a function of the nominal global SFE, the middle row as a function of the local stellar fraction (LSF) reached at the onset of gas expulsion, and the bottom row as a function of the effective gas-expulsion timescale normalized by the stellar crossing time at gas expulsion, $t_{\text{exp}}/t_{\text{cross}}$. Colours represent SFE, symbols connected by lines the $F_{\text{ret,max}}$, and filled stars show the reference MHD models. The LSF orders the impulsive gas-expulsion case, while $t_{\text{exp}}/t_{\text{cross}}$ better explains the adiabatic regime.

sion, making the LSF the parameter that determines survival.

The behaviour changes in the slower gas-expulsion regime, $t_{\text{exp}}/t_{\text{ff}} = 1$, where systems with larger $F_{\text{ret,max}}$ now reach larger bound fractions despite their lower LSF. As discussed in the previous section, increasing $F_{\text{ret,max}}$ raises the stellar velocity dispersion reached during formation and shortens the stellar crossing time at the onset of gas expulsion. The same physical gas-removal timescale therefore becomes effectively more adiabatic from the perspective of the stars, allowing the stellar population more time to adapt to the evolving potential. As a result, systems with stronger embedded contraction can retain a larger bound fraction despite their lower LSF.

The bottom row of Figure 10 shows the bound fraction as a function of $t_{\text{exp}}/t_{\text{cross}}$ at the onset of gas expulsion. In the impulsive regime, $t_{\text{exp}}/t_{\text{ff}} = 0.1$, the different $F_{\text{ret,max}}$ families remain clearly separated, with systems reaching stronger contraction producing systematically lower bound fractions. In this case, the gas-removal timescale remains shorter than $\sim 0.7 t_{\text{cross}}$ for all models, such that survival is regulated mainly by the LSF. In the intermediate regime, $t_{\text{exp}}/t_{\text{ff}} = 0.5$, the separation between $F_{\text{ret,max}}$ families becomes much weaker despite the broad range of stellar crossing times reached by systems with the same SFE, showing that $F_{\text{ret,max}}$ no longer regulates the bound fraction. In this regime, the SFE becomes the dominant parameter controlling survival. Finally, in the slowest gas-expulsion regime, $t_{\text{exp}}/t_{\text{ff}} = 1$, the different $F_{\text{ret,max}}$ families collapse approximately into a single trend as a function of $t_{\text{exp}}/t_{\text{cross}}$. This shows that once the gas-expulsion timescale becomes considerably longer than the stellar dynamical timescale, the stellar response becomes regulated primarily by the local crossing time reached during the embedded phase rather than by the initial cloud free-fall time alone.

Interestingly, the benchmark MHD models appear to lie close to the transition between the impulsive and adiabatic regimes. Their nominal $t_{\text{exp}}/t_{\text{ff}}$ is close to 0.5, while their measured t_{cross} at the onset of gas expulsion is also close to unity, placing them in the regime where the global SFE becomes the main parameter regulating survival. In this context, the low-SFE STARFORGE models naturally reach low bound fractions, while the TORCH models lie in the high-bound-fraction regime where the dependence on both $F_{\text{ret,max}}$ and $t_{\text{exp}}/t_{\text{cross}}$ becomes significantly weaker. However, this balance may shift on different cloud mass scales depending on how efficiently stellar feedback is able to remove the gas from the system.

4. DISCUSSION

Star cluster formation simulations appear to show a common global behaviour. As star formation begins, gas continues collapsing toward the centre of the cloud. This collapse transfers momentum to the newly forming stars while at the same time increasing the central concentration of gas, such that during the embedded phase stars are assembled inside an evolving background potential. This process continues until stellar feedback becomes strong enough to reverse the gas flow and drive the cloud expansion. We have shown that this behaviour is consistent in the two MHD models used here as reference, but we have also explored other MHD simulations showing similar trends, whose analysis will be presented in a future work.

In agreement with seminal studies such as H. Baumgardt & P. Kroupa (2007) and many works that followed, we find that the global structure of the gas during the embedded phase can still be reasonably described by a smooth Plummer-like potential. However, instead of remaining static, the gas distribution contracts while stars are forming, continuously modifying the stellar dynamical state prior to gas expulsion. As gas collapses toward the centre, the stellar fraction decreases while the stellar velocity scale and central concentration increase. The embedded stellar population is therefore not evolving independently from the gas, but dynamically coupled to the global evolution of the cloud.

This behaviour has important consequences for both the survival of young star clusters and the expansion of stellar systems after gas expulsion, all strongly modulated by the gas-expulsion timescale. In the impulsive gas-expulsion regime, the later evolution is determined primarily by the local stellar fraction. As gas collapses, its contribution to the binding potential increases, raising the stellar velocity dispersion before rapidly vanishing. The stellar population is then left in a highly super-virial state, where the expansion rate depends both on how many stars remain bound and on the velocity scale reached during the embedded phase. In this regime, systems reaching larger LSF survive gas expulsion more efficiently.

Interestingly, this behaviour changes once gas expulsion becomes slower. Faster gas contraction decreases the LSF, but at the same time shortens the dynamical timescale of the stellar population by increasing the stellar velocity dispersion. As a result, gas removal becomes effectively more adiabatic from the perspective of the stars in systems reaching stronger contraction. The MHD simulations analyzed here suggest that gas removal occurs closer to the adiabatic regime rather than as an instantaneous event, requiring roughly half

to one free-fall time to effectively clear the gas (J. P. Farias et al. 2023; T. M. Wainer et al. 2025). While these timescales may depend on cloud scale and feedback processes (J. E. Dale et al. 2015; F. Dinmbier & S. Walch 2020), classical studies have already shown that cluster survival depends primarily on the gas-expulsion timescale measured relative to the stellar crossing time (C. J. Lada et al. 1984; M. P. Geyer & A. Burkert 2001; H. Baumgardt & P. Kroupa 2007). In particular, M. P. Geyer & A. Burkert (2001) showed that more concentrated systems survive gas expulsion more efficiently because of their shorter dynamical timescales. In this work, we show that the embedded evolution naturally produces these shorter dynamical times by concentrating gas toward the centre and dynamically heating the stellar population during formation.

Remarkably, both benchmark MHD models lie close to $t_{\text{exp}}/t_{\text{cross}} \sim 1$, near the transition between the impulsive and adiabatic regimes identified in this work. In this regime, the global SFE becomes the main parameter regulating survival, while the dependence on the embedded contraction weakens significantly. It remains to be explored whether other MHD simulations populate the same regime. In this picture, the feedback strength relative to the binding energy of the cloud is not the only quantity governing gas expulsion. The dynamical evolution of the stellar population and its ability to shorten its own dynamical timescale during the embedded phase become equally important, and it is still uncertain which regime is more representative of Galactic star-forming regions.

The heating of the central stellar population also has important consequences for the later expansion of young stellar systems. We have shown that the velocity dispersion reached during the embedded phase is later transformed into bulk expansion motions. However, this transformation is not fully efficient, as part of the embedded kinetic energy can remain stored in bound motions or be redistributed during the relaxation that follows gas expulsion. The efficiency with which this embedded velocity scale is converted into expansion therefore depends both on the boundness of the stellar system and on the gas-expulsion timescale. Current interpretations of expansion in stellar associations remain largely qualitative rather than quantitative. Most expansion diagnostics are designed to determine whether a stellar system is expanding or estimating approximate expansion timescales (N. J. Wright 2018; N. J. Wright & R. J. Parker 2019; M. A. Kuhn et al. 2019; J. J. Armstrong & J. C. Tan 2026), while the connection between these observables and the physical expansion rate of the stellar population has received less attention.

We have shown here that two commonly used expansion metrics are directly connected to the true expansion rate of the stellar population, provided the full kinematic information is available. This opens the possibility of using the expansion of largely unbound systems to recover information about their embedded phase, at least as a lower limit, once these observables are properly calibrated against observational biases. For instance, M. A. Kuhn et al. (2019) measured outward motions in a large sample of young stellar associations, generally finding modest expansion velocities. Similar results have also been found in other Gaia studies of nearby stellar systems (J. J. Armstrong & J. C. Tan 2026; A. D. Croce et al. 2023). Considering that both theoretical and observational evidence point toward low global SFE, such slow outward motions could suggest that gas expulsion was relatively slow compared to the stellar dynamical timescale, reducing the efficiency with which the embedded velocity dispersion is converted into bulk expansion. On the other hand, these low expansion rates may also be affected by observational biases and incompleteness (A. S. M. Buckner et al. 2023), since the fastest and most extended stellar populations are more difficult to identify and a significant fraction of the stellar envelope may already be missing from current samples.

A recent Gaia survey of expansion signatures in nearby young stellar clusters by A. D. Croce et al. (2023) showed that younger systems tend to display stronger expansion signatures than older clusters. In our simulations, however, strongly unbound systems preserve nearly constant expansion metrics over long timescales, while the only clusters that show significant evolution in these metrics are the ones that expand more slowly and contain a larger fraction of bound stars. This suggests that part of the observed weakening of expansion signatures with age may not necessarily reflect the true expansion history of the population, but instead the increasing difficulty of recovering the full stellar envelope at later times, leaving mainly the denser bound component observable. Under this picture, there may exist a limited age window where expansion measurements provide the clearest information about the embedded velocity scale of the stellar population before the expanding envelope becomes too diluted observationally. Following the results of A. D. Croce et al. (2023), this window appears to close at ages of ~ 30 Myr.

This interpretation, however, remains to be tested against observational biases and a more realistic star formation process that must include primordial binaries, stellar evolution and, importantly, substructure. All these processes may contribute to modulating the expansion signatures and bound-cluster thresholds, and

must be explored in future work. In particular, the comparison with the TORCH models suggests that stellar density amplification can depend strongly on how the stellar concentration is measured. While the global velocity amplification is reproduced reasonably well by the simplified framework, global density estimators based on half-mass quantities may underestimate the density reached in local collapsing regions when strong substructure is present. Therefore, the grid of models presented here serves as a baseline to isolate the fundamental dynamical consequences that modern MHD simulations imprint on the stellar populations they produce. In this sense, connecting realistic embedded environments to long-term stellar dynamics becomes necessary to identify which properties of the star formation process are actually preserved in the observable kinematics of young stellar systems.

5. CONCLUSIONS

In this paper, we presented the Dynamical Cluster Assembly Framework (D-CAF), a framework designed to connect embedded star formation histories from MHD simulations to the long-term stellar dynamics of young stellar systems. Using this framework, we constructed a grid of controlled N -body models with evolving background gas potentials to examine how the evolution of the gas and stellar population prior to gas expulsion regulates both the survival and expansion of young stellar systems after gas removal.

Our main results can be summarized as follows:

- The embedded phase is not well represented by a static background potential. Instead, the gas contracts while stars are forming, continuously modifying the stellar dynamical state prior to gas expulsion. As gas collapses toward the centre, the stellar velocity scale and central concentration increase, while the stellar fraction within the embedded region decreases.
- The survival of stellar systems after gas expulsion is strongly regulated by the gas-expulsion timescale. In the impulsive regime, systems become highly supervirial and their later evolution depends primarily on the local stellar fraction reached during the embedded phase. In contrast, once gas removal occurs on timescales comparable to the stellar dynamical time, the response of the stellar system becomes strongly damped and the expansion weakens substantially.
- In the adiabatic gas-expulsion regime, gas contraction shortens the stellar dynamical timescale prior

to gas removal. As a consequence, for a fixed gas-expulsion timescale, systems with stronger contraction experience gas removal in a more adiabatic regime relative to their stellar crossing time. Remarkably, the benchmark MHD models lie close to $t_{\text{exp}}/t_{\text{cross}} \sim 1$, near the transition between the impulsive and adiabatic regimes identified in this work.

- The expansion rate of young stellar systems is not set directly by the SFE itself, but by the stellar velocity scale already present before gas expulsion. In our models, the expansion can only draw from the maximum stellar velocity dispersion reached during the embedded phase, $\sigma_{*,\text{max}}$. The quantity $dR_h/dt/\sigma_{*,\text{max}}$ is thus better interpreted as a measure of how efficiently the natal velocity scale is converted into bulk expansion, rather than as a direct tracer of the natal velocity scale itself. In addition, the comparison with the benchmark STARFORGE models suggests that the assembly history and phase-space coherence of the stellar population may also contribute to the later expansion.
- We examined commonly used observational expansion diagnostics and found that both the velocity-gradient metric κ (when scaled by the true half-mass radius) and the outward velocity directly trace the true expansion rate in the ideal case where full kinematic information is available. In contrast, the ratio $v_R/\sigma(v_r)$ appears to trace how coherent the expansion is relative to the internal velocity dispersion of the system. This result still requires calibration against observational biases. However, it suggests that homogeneous comparisons of expansion strengths between young stellar systems may already provide useful information about their birth environments.
- The expansion rates observed in stellar associations preserve information about their birth environments. In our models, they represent a lower limit on the velocity dispersion reached at the onset of gas expulsion, while the efficiency with which this velocity scale is converted into bulk expansion is regulated by the SFE and the gas-expulsion timescale, particularly in low-SFE systems. In nearly fully unbound associations, the present-day expansion rate of the half-mass radius reaches values of $\sim 70\%$ of the embedded velocity dispersion, decreasing approximately exponentially with gas-expulsion timescale.

These results, however, still need to be tested against observational biases and more realistic star formation processes including primordial binaries, stellar evolution and substructure. Such effects may further modulate both the expansion signatures and the survival of young

stellar systems after gas expulsion. The models presented here provide a baseline to isolate the fundamental dynamical imprint that embedded star formation environments leave on the observable kinematics of young stellar populations.

APPENDIX

A. FITTING THE GAS EVOLUTION FROM RETENTION CURVES

We fit the gas model used in this work from the retention of gas inside a set of fixed initial Lagrangian radii. The goal is to obtain a compact time-dependent Plummer model, with $M_{\text{pl}}(t)$ and $R_{\text{pl}}(t)$, that reproduces the gas evolution in the region that matters dynamically for the stars.

We define the onset time t_0 as the first-star snapshot. At that time, we measure the radii enclosing a fixed set of gas mass fractions f_i . We then keep these radii, r_i , fixed. At later times, we measure how much gas remains inside those same initial radii. This defines the retention curves $F_{\text{ret}}(f_i, t)$ that we use in the fit.

At each snapshot, we approximate the gas with a Plummer sphere with total mass $M_{\text{pl}}(t)$ and scale radius $R_{\text{pl}}(t)$. We write the mass normalization relative to onset as

$$S(t) \equiv \frac{M_{\text{pl}}(t)}{M_0}, \quad (\text{A1})$$

where M_0 is the total gas mass at t_0 . The fit at each snapshot then reduces to the two unknowns $R_{\text{pl}}(t)$ and $S(t)$.

For a trial value of R_{pl} , the model predicts a retention fraction at each fixed shell. At that same R_{pl} , we obtain the best S analytically through a least-squares fit to the measured retention fractions. This reduces the problem to a one-dimensional minimization over R_{pl} . Repeating this step at every snapshot gives the fitted time series $R_{\text{pl}}(t)$ and $S(t)$.

At each snapshot, we fit the retention fractions across all fixed shells to obtain the Plummer scale radius $R_{\text{pl}}(t)$ and a dimensionless mass factor $S(t) = M_{\text{pl}}(t)/M_0$. We then use the enclosed gas masses from all shells and all snapshots together in a second, global least-squares step to determine the single absolute mass scale M_0 . The fitted Plummer mass series then follows from

$$M_{\text{pl}}(t) = M_0 S(t). \quad (\text{A2})$$

The final fitted product is therefore the time series

$$\{t, M_{\text{pl}}(t), R_{\text{pl}}(t)\}. \quad (\text{A3})$$

We then use this table either directly as the tabulated gas background or as the input for the analytic parameterization described in Appendix A.

We fit the retention curves rather than the full gas density profile because they directly track how much gas remains inside the initial star-forming region. This is the part of the gas evolution that enters most directly into the time-dependent gravitational potential felt by the stars.

B. DESCRIPTIVE MODEL FOR THE GAS EVOLUTION

We model the large-scale gas distribution as a spherically symmetric Plummer sphere with time-dependent mass $M_{\text{pl}}(t)$ and scale radius $R_{\text{pl}}(t)$. We use this model as a controlled representation of the gas potential. The goal is not to claim that the gas follows an exact Plummer profile at all times, but to capture the part of the gas evolution that matters most for the stellar dynamics: the large-scale and central depth of the background potential.

At each time, the gas density is

$$\rho(r, t) = \frac{3M_{\text{pl}}(t)}{4\pi R_{\text{pl}}(t)^3} \left(1 + \frac{r^2}{R_{\text{pl}}(t)^2}\right)^{-5/2}, \quad (\text{B4})$$

with enclosed mass

$$M_{\text{pl}}(< r, t) = M_{\text{pl}}(t) \frac{r^3}{(r^2 + R_{\text{pl}}(t)^2)^{3/2}}. \quad (\text{B5})$$

In the workflow used here, this gas model appears in two forms. In the tabulated version, we fit the MHD gas evolution snapshot by snapshot (see Appendix A) and use the resulting time series

$$t, \quad M_{\text{pl}}(t), \quad R_{\text{pl}}(t) \quad (\text{B6})$$

directly into the N -body calculation as background potential. In the parameterized version, we replace this fitted sequence by a compact analytic model that captures the same broad behaviour with a small number of parameters.

We anchor the analytic model at the onset of star formation, t_0 , defined as the first-star snapshot. The parameterized model assumes two phases: an embedded contraction phase, followed by a post-peak expansion phase. For $t \leq t_{\text{ge}}$, we write

$$R_{\text{pl}}(t) = R_{\text{pl}0} \sqrt{1 - \frac{t - t_0}{t_{\text{col}}}}, \quad (\text{B7})$$

where $R_{\text{pl}0}$ is the onset scale radius and t_{col} is the collapse timescale. For $t > t_{\text{ge}}$, we switch to an exponential expansion,

$$R_{\text{pl}}(t) = R_{\text{pl}}(t_{\text{ge}}) \exp\left(\frac{t - t_{\text{ge}}}{t_{\text{exp}}}\right), \quad (\text{B8})$$

where t_{exp} controls how rapidly the gas potential opens after the collapse has reached its maximum concentration.

For the gas mass, we use a simple piecewise function,

$$M_{\text{pl}}(t) = M_0 + \dot{M}(t - t_0), \quad t \leq t_{\text{ge}}, \quad (\text{B9})$$

and

$$M_{\text{pl}}(t) = M_{\text{pl}}(t_{\text{ge}}), \quad t > t_{\text{ge}}. \quad (\text{B10})$$

In the parameterized runs used in this work, we take $\dot{M} = 0$, so the mass remains constant and the time dependence enters mainly through $R_{\text{pl}}(t)$.

We determine the parameters of this model from the shell-based retention analysis of the original MHD simulation. We use the onset properties to fix $R_{\text{pl}0}$ and M_0 , and we use the peak of the retention curve at a chosen calibration shell to define t_{ge} and the maximum retention factor $F_{\text{ret,max}}$. In this work, we take the calibration shell to be the initial 10% gas Lagrangian radius, so that $f_{\text{cal}} = 0.1$ and r_{cal} is the radius enclosing that fraction at t_0 . In this formulation, $F_{\text{ret,max}}$ is the quantity used to set the maximum contraction, while the collapse timescale t_{col} is derived from it. For $\dot{M} = 0$, the value of $F_{\text{ret,max}}$ fixes the Plummer radius at the transition time,

$$R_{\text{pl}}(t_{\text{ge}}) = r_{\text{cal}} \sqrt{(f_{\text{cal}} F_{\text{ret,max}})^{-2/3} - 1}, \quad (\text{B11})$$

and the collapse timescale then follows from

$$t_{\text{col}} = \frac{t_{\text{ge}} - t_0}{1 - (R_{\text{pl}}(t_{\text{ge}})/R_{\text{pl}0})^2}. \quad (\text{B12})$$

We then determine the remaining timescale t_{exp} by comparing the post-peak retention tail of the analytic model to the measured retention curves and selecting the value that minimizes the residual.

The final parameterized background is therefore specified by the set

$$\{R_{\text{pl}0}, M_0, t_{\text{ge}}, F_{\text{ret,max}}, t_{\text{exp}}\}, \quad (\text{B13})$$

with t_{col} derived from these quantities, and with $\dot{M} = 0$ in the runs used here. This provides a compact description of the gas evolution that preserves the three features that matter most dynamically: the initial depth of the potential, the amount of contraction before gas expulsion, and the timescale over which the background potential opens afterward.

REFERENCES

- Armstrong, J. J., & Tan, J. C. 2026, Expansion Kinematics of Young Clusters. III. The Kiloparsec Sample, doi: [10.48550/arXiv.2604.08422](https://doi.org/10.48550/arXiv.2604.08422)
- Barnes, J., & Hut, P. 1986, Nature, 324, 446, doi: [10.1038/324446a0](https://doi.org/10.1038/324446a0)

- Baumgardt, H., & Kroupa, P. 2007, *MNRAS*, 380, 1589, doi: [10.1111/j.1365-2966.2007.12209.x](https://doi.org/10.1111/j.1365-2966.2007.12209.x)
- Bressert, E., Bastian, N., Gutermuth, R., et al. 2010, *MNRAS*, 409, L54, doi: [10.1111/j.1745-3933.2010.00946.x](https://doi.org/10.1111/j.1745-3933.2010.00946.x)
- Buckner, A. S. M., Naylor, T., Dobbs, C. L., Rieder, S., & Bending, T. J. R. 2023, *Monthly Notices of the Royal Astronomical Society*, 527, 5448, doi: [10.1093/mnras/stad3367](https://doi.org/10.1093/mnras/stad3367)
- Cournoyer-Cloutier, C., Tran, A., Lewis, S., et al. 2020, *MNRAS*, In Prep, 1
- Cournoyer-Cloutier, C., Sills, A., Harris, W. E., et al. 2024, *The Astrophysical Journal*, 977, 203, doi: [10.3847/1538-4357/ad90b3](https://doi.org/10.3847/1538-4357/ad90b3)
- Croce, A. D., Dalessandro, E., Livernois, A. R., & Vesperini, E. 2023, *Young, Wild and Free: The Early Expansion of Star Clusters*, arXiv, doi: [10.48550/arXiv.2312.02263](https://doi.org/10.48550/arXiv.2312.02263)
- Dale, J. E., Ercolano, B., & Bonnell, I. A. 2013, *MNRAS*, 430, 234, doi: [10.1093/mnras/sts592](https://doi.org/10.1093/mnras/sts592)
- Dale, J. E., Ercolano, B., & Bonnell, I. A. 2015, *MNRAS*, 451, 987, doi: [10.1093/mnras/stv913](https://doi.org/10.1093/mnras/stv913)
- Dinbier, F., & Walch, S. 2020, *MNRAS*, 499, 748, doi: [10.1093/mnras/staa2560](https://doi.org/10.1093/mnras/staa2560)
- Elmegreen, B. G. 2007, *ApJ*, 668, 1064, doi: [10.1086/521327](https://doi.org/10.1086/521327)
- Farias, J. P., Fellhauer, M., Smith, R., Domínguez, R., & Dabringhausen, J. 2018, *MNRAS*, 476, 5341, doi: [10.1093/mnras/sty597](https://doi.org/10.1093/mnras/sty597)
- Farias, J. P., Offner, S. S. R., Grudić, M. Y., Guszejnov, D., & Rosen, A. L. 2023, *Mon. Not. R. Astron. Soc.*, 527, 6732, doi: [10.1093/mnras/stad3609](https://doi.org/10.1093/mnras/stad3609)
- Farias, J. P., Smith, R., Fellhauer, M., et al. 2015, *MNRAS*, 450, 2451, doi: [10.1093/mnras/stv790](https://doi.org/10.1093/mnras/stv790)
- Farias, J. P., & Tan, J. C. 2023, *Monthly Notices of the Royal Astronomical Society*, 523, 2083, doi: [10.1093/mnras/stad1532](https://doi.org/10.1093/mnras/stad1532)
- Farias, J. P., Tan, J. C., & Chatterjee, S. 2019, *MNRAS*, 483, 4999, doi: [10.1093/mnras/sty3470](https://doi.org/10.1093/mnras/sty3470)
- Federrath, C., & Klessen, R. S. 2012, *ApJ*, 761, 156, doi: [10.1088/0004-637X/761/2/156](https://doi.org/10.1088/0004-637X/761/2/156)
- Fryxell, B., Olson, K., Ricker, P., et al. 2000, *The Astrophysical Journal Supplement Series*, 131, 273, doi: [10.1086/317361](https://doi.org/10.1086/317361)
- Fujii, M., Iwasawa, M., Funato, Y., & Makino, J. 2007, *Publ. Astron. Soc. Japan*, 59, 1095, doi: [10.1093/pasj/59.6.1095](https://doi.org/10.1093/pasj/59.6.1095)
- Fujii, M. S., & Zwart, S. P. 2011, *Science*, 334, 1380, doi: [10.1126/science.1211927](https://doi.org/10.1126/science.1211927)
- Geyer, M. P., & Burkert, A. 2001, *MNRAS*, 323, 988, doi: [10.1046/j.1365-8711.2001.04257.x](https://doi.org/10.1046/j.1365-8711.2001.04257.x)
- Goodwin, S. P., & Bastian, N. 2006, *MNRAS*, 373, 752, doi: [10.1111/j.1365-2966.2006.11078.x](https://doi.org/10.1111/j.1365-2966.2006.11078.x)
- Grudić, M. Y., Diederik Kruijssen, J. M., Faucher-Giguère, C. A., et al. 2021a, *Mon. Not. R. Astron. Soc.*, 506, 3239, doi: [10.1093/mnras/stab1894](https://doi.org/10.1093/mnras/stab1894)
- Grudić, M. Y., Guszejnov, D., Hopkins, P. F., et al. 2018, *Mon. Not. R. Astron. Soc.*, 481, 688, doi: [10.1093/mnras/sty2303](https://doi.org/10.1093/mnras/sty2303)
- Grudić, M. Y., Guszejnov, D., Hopkins, P. F., Offner, S. S. R., & Faucher-Giguère, C.-A. 2021b, *Mon. Not. R. Astron. Soc.*, 506, 2199, doi: [10.1093/mnras/stab1347](https://doi.org/10.1093/mnras/stab1347)
- Grudić, M. Y., Hopkins, P. F., Lee, E. J., et al. 2019, *Monthly Notices of the Royal Astronomical Society*, 488, 1501, doi: [10.1093/mnras/stz1758](https://doi.org/10.1093/mnras/stz1758)
- Guszejnov, D., Grudić, M. Y., Hopkins, P. F., Offner, S. S. R., & Faucher-Giguère, C.-A. 2021, *Mon. Not. R. Astron. Soc.*, 502, 3646, doi: [10.1093/mnras/stab278](https://doi.org/10.1093/mnras/stab278)
- Guszejnov, D., Grudić, M. Y., Offner, S. S. R., et al. 2022, *Monthly Notices of the Royal Astronomical Society*, 515, 4929, doi: [10.1093/mnras/stac2060](https://doi.org/10.1093/mnras/stac2060)
- Guszejnov, D., Raju, A. N., Offner, S. S. R., et al. 2023, *Mon. Not. R. Astron. Soc.*, 518, 4693, doi: [10.1093/mnras/stac3268](https://doi.org/10.1093/mnras/stac3268)
- Hopkins, P. F. 2015, *Mon. Not. R. Astron. Soc.*, 450, 53, doi: [10.1093/mnras/stv195](https://doi.org/10.1093/mnras/stv195)
- Hopkins, P. F., & Raives, M. J. 2016, *Mon. Not. R. Astron. Soc.*, 455, 51, doi: [10.1093/mnras/stv2180](https://doi.org/10.1093/mnras/stv2180)
- Kroupa, P. 2002, *Science (80-.)*, 295, 82, doi: [10.1126/SCIENCE.1067524](https://doi.org/10.1126/SCIENCE.1067524)
- Kuhn, M. A., Hillenbrand, L. A., Sills, A., Feigelson, E. D., & Getman, K. V. 2019, *The Astrophysical Journal*, 870, 32, doi: [10.3847/1538-4357/aaef8c](https://doi.org/10.3847/1538-4357/aaef8c)
- Lada, C. J., & Lada, E. A. 2003, *Annu. Rev. Astron. Astrophys.*, 41, 57, doi: [10.1146/annurev.astro.41.011802.094844](https://doi.org/10.1146/annurev.astro.41.011802.094844)
- Lada, C. J., Margulis, M., & Dearborn, D. 1984, *ApJ*, 285, 141, doi: [10.1086/162485](https://doi.org/10.1086/162485)
- Lee, P. L., & Goodwin, S. P. 2016, *MNRAS*, 460, 2997, doi: [10.1093/mnras/stw988](https://doi.org/10.1093/mnras/stw988)
- MacLow, M.-M. 2004, *Astrophys. Space Sci.*, 289, 323, doi: [10.1023/B:ASTR.0000014961.72318.7c](https://doi.org/10.1023/B:ASTR.0000014961.72318.7c)
- Moeckel, N., & Bate, M. R. 2010, *MNRAS*, 404, 721, doi: [10.1111/j.1365-2966.2010.16347.x](https://doi.org/10.1111/j.1365-2966.2010.16347.x)
- Parker, R. J., Goodwin, S. P., & Allison, R. J. 2011, *MNRAS*, 418, 2565, doi: [10.1111/j.1365-2966.2011.19646.x](https://doi.org/10.1111/j.1365-2966.2011.19646.x)
- Parker, R. J., Wright, N. J., Goodwin, S. P., & Meyer, M. R. 2014, *MNRAS*, 438, 620, doi: [10.1093/mnras/stt2231](https://doi.org/10.1093/mnras/stt2231)

- Pavlík, V. 2020, *A&A*, 638, 1,
doi: [10.1051/0004-6361/202037490](https://doi.org/10.1051/0004-6361/202037490)
- Pelupessy, F. I., Van Elteren, A., De Vries, N., et al. 2013, *A&A*, 557, A84, doi: [10.1051/0004-6361/201321252](https://doi.org/10.1051/0004-6361/201321252)
- Pokhrel, R., Gutermuth, R. A., Betti, S. K., et al. 2020, *Astrophys. J.*, 896, 60, doi: [10.3847/1538-4357/ab92a2](https://doi.org/10.3847/1538-4357/ab92a2)
- Portegies Zwart, S., McMillan, S. L., Van Elteren, A., Pelupessy, F. I., & De Vries, N. 2013, *Comput. Phys. Commun.*, 184, 456, doi: [10.1016/j.cpc.2012.09.024](https://doi.org/10.1016/j.cpc.2012.09.024)
- Quintana, A. L., Wright, N. J., Kormann, L. A., et al. 2025, A New Gaia Census of OB Associations within 1 Kpc, arXiv, doi: [10.48550/arXiv.2512.05854](https://doi.org/10.48550/arXiv.2512.05854)
- Smith, R., Slater, R., Fellhauer, M., Goodwin, S., & Assmann, P. 2011, *MNRAS*, 416, 383, doi: [10.1111/j.1365-2966.2011.19039.x](https://doi.org/10.1111/j.1365-2966.2011.19039.x)
- Springel, V. 2005, *MNRAS*, 364, 1105, doi: [10.1111/j.1365-2966.2005.09655.x](https://doi.org/10.1111/j.1365-2966.2005.09655.x)
- Wainer, T. M., Dalcanton, J. J., Grudić, M. Y., et al. 2025, The Timescales of Embedded Star Formation as Observed in STARFORGE, arXiv, doi: [10.48550/arXiv.2509.18322](https://doi.org/10.48550/arXiv.2509.18322)
- Wall, J. E., Low, M.-M. M., McMillan, S. L. W., et al. 2020, *Astrophys. J.*, 904, 192, doi: [flash](https://doi.org/flash)
- Wall, J. E., McMillan, S. L. W., Mac Low, M.-M., Klessen, R. S., & Zwart, S. P. 2019,
- Wang, L., Iwasawa, M., Nitadori, K., & Makino, J. 2020, *Monthly Notices of the Royal Astronomical Society*, 497, 536, doi: [10.1093/mnras/staa1915](https://doi.org/10.1093/mnras/staa1915)
- Wright, N. J. 2018, doi: [10.5281/ZENODO.1489060](https://doi.org/10.5281/ZENODO.1489060)
- Wright, N. J., & Parker, R. J. 2019, *Mon. Not. R. Astron. Soc.*, 489, 2694, doi: [10.1093/mnras/stz2303](https://doi.org/10.1093/mnras/stz2303)